ELSEVIER

Contents lists available at ScienceDirect

Chemical Engineering Journal

journal homepage: www.elsevier.com/locate/cej





Orbital occupancy modulation to optimize the electroactivity towards bidirectional sulfur conversion in lithium-sulfur batteries

Wei Zhou a,c , Zilong Li b , Shunlian Ning d , Jinchang Xu e , Ming-Hsien Lee f , Dengke Zhao a,* , Jian Qing b,* , Nan Wang b , Hui Meng b

- ^a School of Materials Science and Engineering, Henan Normal University, Xinxiang, Henan 453007, China
- ^b Siyuan laboratory, Guangzhou Key Laboratory of Vacuum Coating Technologies and New Energy Materials, Guangdong Provincial Engineering Technology Research Center of Vacuum Coating Technologies and New Energy Materials, Guangdong Provincial Key Laboratory of Nanophotonic Manipulation, Department of Physics, Jinan University, Guangzhou 510632, China
- ^c BYD Auto Industry Company Limited, Shenzhen, Guangdong 518000, China
- ^d School of Chemistry, Sun Yat-sen University, Guangzhou, Guangdong 510275, China
- ^e Guangdong Provincial Key Laboratory of Terahertz Quantum Electromagnetics, GBA Branch of Aerospace Information Research Institute, Chinese Academy of Sciences, Guangzhou 510700, Guangdong, China
- f Department of Physics, Tamkang University, New Taipei 25137, Taiwan

ARTICLE INFO

Keywords: Lithium-sulfur battery Fe-Co₉S₈@CNT Electronic regulation e_g orbit occupancy

ABSTRACT

Exploring a simple way to simultaneously modulate the electronic structure and physical architecture of metal sulfides can contribute to improve their electroactivity for bidirectional sulfur conversion in lithium-sulfur batteries (LSBs). Herein, a novel Fe cluster modified Co_9S_8 supported on hollow carbon nanotube (Fe-Co $_9\text{S}_8$ @CNT) is prepared for LSBs by one-step self-vulcanizing/doping. The X-ray absorption spectroscopy and in-situ Raman spectra reveal the formation of Fe—Co bonds leads to Co_9S_8 with abundant S vacancy, thereby effectually regulating the electronic structure of Co sites to enhance the adsorption and conversion polysulfides. Moreover, the well-developed porous and hollow structure facilitate the storage of active S and the mass transfer. Therefore, the S/Fe-Co $_9\text{S}_8$ @CNT cathode indicates a favorable rate capability (775.7 mAh g $^{-1}$ at 5.0C) and cycling stability (capacity attenuation of 0.022 % each cycle at 3.0C over 1000 cycles). Density functional theory further elucidates the underlying cause of the excellent electroactivity, confirming Fe doping reduces the occupancy of e_g orbit of Co sites from 3.81 to 3.6, which can facilitate formation of suitable bond orders between Co site and Li $_2\text{S}_x$, thus lowering the energy barrier of rate-determining step. This work supplies an available way to the design of excellent S hosts for LSBs.

1. Introduction

LSBs with a high theoretical gravimetric energy density (2600 Wh ${\rm kg}^{-1}$) are generally regarded as one of most ideal potential energy storage devices to meet the growing demand for energy from electric vehicles and portable electronics [1,2]. However, their practical use is presently constrained by the sluggish S conversion reaction and grievous "shuttle effect" of lithium polysulfides (LiPSs) intermediates [3,4], which often leads to large polarization, poor rate performance and accelerated capacity degradation in LSBs [5,6]. A substantial body of studies indicates that the utilization of electrocatalysts within LSBs constitutes a straightforward method to overcome mentioned problem [7,8]. In this case, low-cost cobalt sulfides (${\rm CoS}_{\rm x}$) are regarded as one of

the most promising candidate materials, owing to their excellent conductivity and tunable electronic structure [9,10]. Nevertheless, S redox reaction involves multiple electron transfer, common CoS_x limited by intrinsic activity, poor specific surface area and low accessible active sites, how to achieve the rapid transformation of LiPSs and inhibiting their dissolution under harsh conditions ((S loading >4 mg cm $^{-2}$, E/S < $10~\mu L$ mg $^{-1}$)) still pose a challenge. To counter this, it is imperative to explore viable strategies for further increase activity of CoS_x .

In the context of a multi-step electrochemical reaction, the rate of reaction is predominantly contingent upon the energy barrier (ΔG_{RDS}) of the rate-determining step (RDS). For 3d group metal compound, the ΔG_{RDS} can be reduced by reasonably modulating the 3d electron structure of catalysts [11]. According to molecular orbital hybridization

E-mail addresses: zhaodengke@htu.edu.cn (D. Zhao), qingjian@jnu.edu.cn (J. Qing), nanwang@email.jnu.edu.cn (N. Wang).

https://doi.org/10.1016/j.cej.2025.167290

Received 7 March 2025; Received in revised form 7 August 2025; Accepted 14 August 2025 Available online 15 August 2025

^{*} Corresponding authors.

theory, for CoS_v as an electrocatalyst to catalyze the S redox reaction, the adsorption of LiSx on Co sites is realized by the interaction between 3d orbitals of Co and 3p orbitals of the LiSx [12], and the adsorption strength of LiS_x determines the level of ΔG_{RDS} . This can be analyzed by the bond order of bonding and anti-bonding orbitals. In principle, a lower anti-bonding orbital occupancy will lead to an enhanced adsorption capacity. Furthermore, crystal field theory demonstrates that 3d orbitals can be spited into t_{2g} (d_{xy} , d_{yz} and d_{xz}) and e_g (d_{x2} , q_{yz} , d_{zz}) orbitals, where the filling of e_g is significant for the anti-bonding orbital occupancy and formation of intermediates due to it has a substantial degree of vertical overlap with pz orbitals. Therefore, electrocatalytic performance of CoS_x can be improved by the modulation of e_g orbital occupancy. Recently, many efforts find that doping high-valence metal ions (V, Fe, Mo and so on) with a multitude of unoccupied d orbitals into host materials can adjust their e_g orbital occupancy by the formation of robust strong d-π-conjugated system, thereby enhancing their electroactivity [13-15]. For example, Wu et al. regulated the spin state of Co₉S₈ by V doping, thereby optimizing the adsorption/desorption of intermediates to significantly increase the oxygen catalytic activity [16]. It can thus be concluded that the precise modulation of the d-orbital electronic configuration of the Co site in CoS_v through high-valence metal doping may lead to a further enhancement of the intrinsic activity towards sulfur-involved reactions. Moreover, combining with the various characterizations and theoretical analysis to reveal the structure-activity relationship between activity and electronic structure will further encourage the advancement of electrocatalysts for LSBs.

In addition to excellent electroactivity, the three-dimensional (3D) physical architecture is also an important factor for enhancing the performance of the S cathode. Hollow nanoreactor with high surface-tovolume ratios are considered one of the most ideal structures, which can not only expose more active sites, but also can provide additional storage space for S, alleviate the issue of S volume expansion, and enhance mass transfer [17,18]. Inspired by these principles, a wellstructured hollow nanoreactor composed of Fe cluster modified Co₉S₈ nanoparticles (NPs) and hollow carbon nanotube (Fe-Co₉S₈@CNT) is prepared as a S cathode material by annealing-self-vulcanizing-doping strategy. Characterization results indicate that the hollow structure ensures a high sulfur (S) loading, mitigates volume expansion, expedites mass transfer, and increases the number of accessible active sites. Moreover, the in-situ formed Fe-Co bonds optimize the d-orbital electronic configuration of Co₉S₈ and induce a high density of sulfur vacancies (V_S), thus enhancing the bidirectional sulfur conversion performance. The in-situ Raman spectra recorded during the charge/ discharge process further corroborate these results, where no distinct signals of LiPSs can be found, further suggesting the high electroactivity of Fe-Co₉S₈@CNT. So, S/Fe-Co₉S₈@CNT cathode indicates remarkable battery performance, including high capacity of 775.7 mAh g⁻¹ at 5.0C and an ultralow capacity attenuation with 0.022 % each cycle at 3.0C over 1000 cycles. Even under high S loading of 15.4 mg cm⁻² and poor E/S of 6.0 μL mg⁻¹, the S/Fe-Co₉S₈@CNT cathode still exhibits the high initial areal capacity of 15.44 mAh cm⁻² at 0.2C and excellent cycle stability with 86.8 % capacity reservation after 100 cycles. Density functional theory (DFT) demonstrates that Fe doping reduces the occupancy of the $e_{\rm g}$ orbit and the bandgap of Co_9S_8 , which leads to more stable bond orders (BOs) between Co₉S₈ and Li₂S_x, thus lowering the ΔG_{RDS} to improve the catalytic performance.

2. Experimental section

2.1. Preparation of 1D CdS nanowires (CdS NWs)

The uniform CdS NWs were prepared by the solvothermal way. Summarily, cadmium diethyldithiocarbamate $(Cd(S_2CNEt_2)_2)$ was obtained via co-precipitation of cadmium chloride (2.1 g) and sodium diethyldithiocarbamate trihydrate (2.5 g). Subsequently, the mixture of $Cd(S_2CNEt_2)_2$ (1.688 g) was transferred into 100 mL of Teflon-lined

stainless autoclave containing 80 mL ethylenediamine, which was kept at 180 °C for 24 h. After cooling naturally to room temperature, the bright yellow precipitate was achieved via centrifugation and washed with $\rm H_2O$ for 3 times and finally dried at 70 °C for 12 h.

2.2. Preparation of CdS@Fe-PDA NWs

The 200 mg of as-fabricated CdS NWs and 1.5 wt% FeCl $_3$ were dissolved into 100 mL $_2$ O with stirring for 5 min. And then 1 mL of ammonia (25–28 %) was added into the solution described above. After stirring for 10 min, 10 mL hydrochloride (DA, 20 mg mL $^{-1}$) was slowly dripped into the above mixture and stirred continuously at room temperature for 12 h. The CdS@Fe-PDA NWs were obtained by centrifugation and washed with $_{2}$ O for 3 times.

2.3. Preparation of CdS@Fe-PDA@ZIF-67 NWs

The as-fabricated CdS@Fe-PDA NWs (7.97 g) and Co(NO $_3$) $_2$ •6H $_2$ O (2.45 g) were dispersed in methanol solution (180 mL). Then, the 1.2 g of 2-methylimidazole (2-MIM) was dissolved methanol solution (20 mL) and quickly poured into the above solution and stirred for 3 h at 30 °C. The CdS@Fe-PDA@ZIF-67 NWs was obtained by filtration and washed with methanol for 3 times.

2.4. Preparation of Fe-Co₉S₈@CNT

The 100 mg of as-fabricated precursors were placed into the middle of the tube furnace and heated at 1000 $^{\circ}$ C for 3 h under Ar atmosphere and then acid etching was conducted to obtain the Fe-Co₉S₈@CNT.

2.5. Preparation of other materials

The $\text{Co}_9S_8@\text{CNT}$, and Fe@CNT materials were fabricated via the same step of the Fe/Co $_9S_8@\text{CNT}$ except that the precursors were CdS@Fe-PDA@ZIF-67 NWs and CdS@Fe-PDA NWs, respectively.

2.6. Preparation of S/Fe-Co₉S₈@CNT

The Fe-Co₉S₈@CNT and S powder (the weight ratio is 2:8) were evenly mixed and then was transferred into the middle of the tube furnace. Subsequently, the mixture was heated at 155 $^{\circ}$ C for 12 h and further 200 $^{\circ}$ C for 60 min with N₂ atmosphere. For comparison, the S/Co₉S₈@CNT and S/Fe@CNT were synthesized through the analogous method.

2.7. Materials characterization

The morphological and structural characteristics were performed via the Scanning electron microscopy (SEM, Gemini FE-SEM) and transmission electron microscopy (TEM, JEM-2100HR). The X-ray diffractometer (XRD, Rigaku-D/Max-IIIA) and X-ray photoelectron spectroscopy (XPS, Thermo-ESCA-Lab 250) were employed to investigate the structural information of the as-fabricated materials. The inVia Qontor Raman Spectrometer was used to analyze the Raman spectra. The Kubo-X1000 instrument was employed to perform the Brunauer-Emmett-Teller (BET) and $\rm N_2$ adsorption–desorption isotherms. Thermogravimetric analysis (TGA, Netzsch STA 449C) in $\rm N_2$ atmosphere was used to estimate the sulfur mass content of the as-prepared composites. The adsorption performances of LiPSs were conducted by the UV–Vis spectrophotometer (UV2600 2200 CH).

2.8. Electrochemical measurements

The super P, Polyvinylidene fluoride (PVDF), and electroactive materials with the weight ratio of 2:1:7 were uniformly dispersed into N-methyl-2-pyrrolidene (NMP) under stirring continuously for 8.0 h and

followed obtained the uniform slurry. Subsequently, the fabricated slurry was uniformly covered on the Al foil and dried at 60 $^{\circ}$ C for 12 h. The coin batteries (CR2032) were assembled in the glovebox, which is composed of the cathode part (S/Fe-Co_9S_8@CNT), anode part (lithium metal), the separator (Celgard 2400), and a commonly used Li—S battery electrolyte with 2 % LiNO_3. Particularly, when the cathode with low or high sulfur areal loading, the ratios of electrolyte and sulfur (E/S) were 15 μL mg $^{-1}$ or 6 μL mg $^{-1}$, respectively. Cycling properties of the batteries were conducted on a Land CT2001A instrument, where the voltage range was 1.7–2.8 V. Other electrochemical performances such like CV curves and EIS were performed via electrochemical workstation CHI 760E. Galvanostatic intermittent titration (GITT) measurements were operated with the current pulse for 10 min at 0.2 mA and then rested 1 h.

2.9. Li₂S₆ adsorption experiments

The 5 mM Li $_2S_6$ solution was synthesized by mixing S and Li $_2S$ (the molar ratio: 5:1) in the tetrahydrofuran (THF) solvent with stirring for overnight in the glovebox. Subsequently, 10 mg Fe-Co $_9S_8$ @CNT, Co $_9S_8$ @CNT and Fe@CNT powders were placed into the Li $_2S_6$ solution, respectively. The color change of Li $_2S_6$ solution illustrates the adsorption ability of the host materials to polysulfides.

2.10. Symmetrical-cell assembly and experiments

2.11. Li₂S nucleation and dissolution measurements

A 0.2 M Li $_2$ S $_8$ solution was formed via mixing S and Li $_2$ S (the molar ratio: 7:1) in tetraglyme solvent under stirring overnight. The assynthesized Li $_2$ S $_8$ (25 μ L) was employed as catholyte and the commonly used Li—S battery electrolyte with 2 % LiNO $_3$ (25 μ L) was employed as anolyte. Nucleation of Li $_2$ S measurements were carried out with lithium anode as the counter electrode and the as-synthesized cathodes as the working electrode. The assembled cells were first galvanostatically discharged to 2.06 V at 0.112 mA and followed potentiostatically discharged at 2.05 V until the current was below 0.01 mA. For the Li $_2$ S dissolution measurements, the cells were galvanostatically discharged to 1.7 V at 0.01C and then potentiostatically charged until the current was less than 0.01 mA at 2.4 V.

2.12. Linear sweep voltammetry (LSV) measurements

The Fe-Co₉S₈@CNT electrocatalysts towards LiPSs were further illustrated by linear sweep voltammetry (LSV) measurements and derivative Tafel plots. The Li-catalyst asymmetric battery was synthesized by the analogous procedures as the nucleation measurements. The LSV curves were performed at the scan rate of 5.0 mVs⁻¹ with the voltage range 2.3 V to 1.5 V. Tafel plots were evaluated based on the data of LSV curves, as depicted in the following equation V = a + blogj, where the b displays the Tafel slope and j represents the current density in LSV curves.

2.13. Density functional theory (DFT)

DFT calculations were carried out with the open source planewave code (Quantum Espresso). For all calculations, the spin polarized

generalized gradient approximation (GGA) of the ultrasoft pseudopotentials and Perdew–Burke–Ernzerhof (PBE) functional were employed for the core electrons. Furthermore, the plane-wave cut off energy was "fine". The energy and convergence of forces on each atom at structure relaxation were $10^{-6}~\mbox{eV}$ in energy and $0.04~\mbox{eV}$ Å $^{-1}$ in force, respectively. The $3\times3\times1$ Monkhorst-Pack k-point grid was used to sample the Brillouin zone. To prevent interplanar interactions, the vacuum space in the z-direction was surpass15 Å. The top two layers were permitted to relax about the optimization of geometric models. The adsorption energies (E_a) for sulfur species on the Fe-Co₉S₈ or Co₉S₈ surfaces are regarded as $E_a = E_{total} - E_{ads} - E_{slab}$, in which E_{total} means all energy of the adsorbed system, E_{ads} represents the energy of the adsorbate sulfur species in vacuum and E_{slab} indicates the energy of the optimized clean surface slab.

3. Results and discussion

The fabrication process of the Fe-Co₉S₈@CNT is schematically elaborated in Fig. 1a, with further details provided in the experimental section. Initially, dopamine hydrochloride (DA) is polymerized in the presence of FeCl₃ and CdS NWs to prepare CdS@Fe-PDA NWs, where the CdS NWs are served as self-sacrificing templates and S source. Subsequently, adding ${\rm Co}^{2+}$ ions and 2-MIM to form CdS@Fe-PDA@ZIF-67 NWs. Finally, Fe-Co₉S₈@CNT is obtained by the annealing of the precursor under the Ar atmosphere. For purposes of comparison, the Co₉S₈@CNT and Fe@CNT are also prepared by the same procedure, without the addition of FeCl₃ and ZIF-67, respectively.

The morphology of as-prepared samples is analyzed by scanning electron microscopy (SEM) and transmission electron microscopy (TEM). Fig. 1b illustrates that the as-prepared CdS NWs indicate uniform one-dimensional (1D) nanowires topography with a diameter of approximately 50 nm. As illustrated in Fig. S1a-c and Fig. 1c-d, CdS@Fe-PDA NWs, CdS@Fe-PDA@ZIF-67 NWs, Co₉S₈@CNT and Fe-Co₉S₈@CNT also express a uniform 1D morphology. Because of the decomposition of CdS NWs, in TEM image (Fig. 1e and Fig. S2), Fe-Co₉S₈@CNT displays the obvious hollow nanotube structure. Additionally, some NPs can be observed in the nanotube. In the corresponding SAED pattern (Fig. S1d), a distinct set of diffraction rings of (111), (311), (511), and (440) planes of cubic phase Co₉S₈ can be observed, suggesting that formation of Co₉S₈ NPs. Moreover, the absence of an evident diffraction ring associated with Fe species or CdS can be observed, indicating that they may exist in the form of single atoms or clusters, or alternatively, have undergone complete volatilization. HRTEM image (Fig. 1f, g) corroborates the aforementioned findings, wherein the lattices with a spacing of 0.34 and 0.30 nm are discernible, corresponding to the graphite carbon (002) plane and the cubic Co₉S₈ (311) plane. Additionally, the surface exhibits a multitude of defects. The EDS elemental mapping images of Fe-Co₉S₈@CNT (Fig. 1h) indicate the presence of C, N, O, Co, S, and Fe element but no Cd element, which demonstrates that the CdS NWs have undergone complete volatilization during the annealing process. It is noteworthy that the C, N, and O elements are distributed in a uniform manner throughout the sample, while the dispersion of the Co and S elements exhibits a high degree of overlap with the nanoparticles, suggesting that the predominant composition of the nanoparticle is Co and S. Moreover, it can be found that the distribution of the Fe element is analogous to that of Co and S, demonstrating that the Fe mainly modified on Co₉S₈, and the generation of defects in Co₉S₈ may be attributed to Fe doping. Moreover, to clearly determine the amount of metal in Fe-Co₉S₈@CNT, ICP-OES measurement further is performed, more detail can be seen in Tables S1, the content of Fe and Co are 2.2 and 14.8 wt%, respectively.

More details of structural information of the as-prepared samples are conducted via X-ray diffraction (XRD) patterns. As depicted in Fig. S3a, all XRD patterns express a broad peak located at 26° , corresponding to the (002) facets of graphitic carbon [19]. In addition, Fe-Co₉S₈@CNT and Co₉S₈@CNT deliver extra diffraction peaks located at 15.8, 29.5,

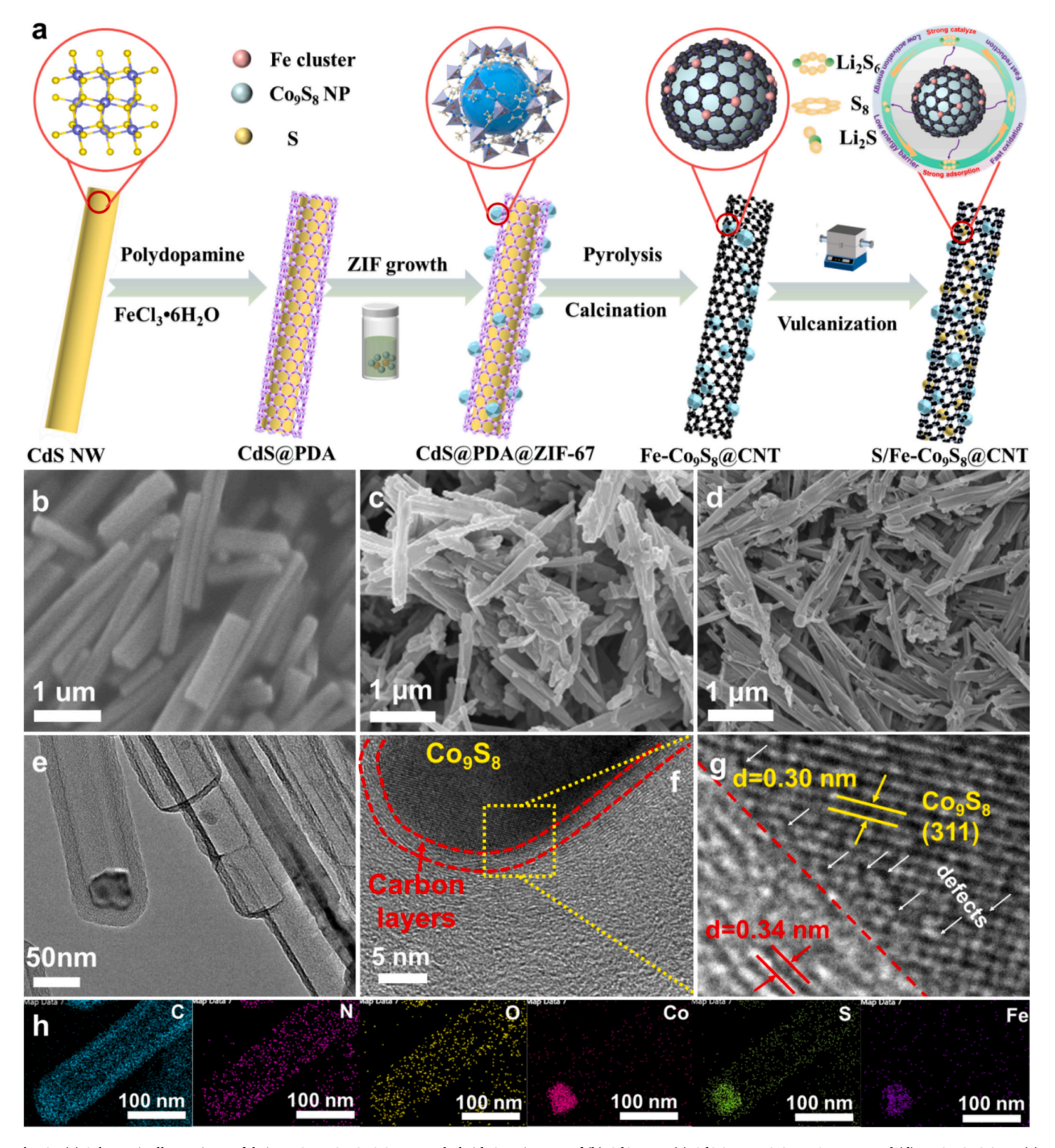


Fig. 1. (a) Schematic Illustration to fabricate S/Fe-Co₉S₈@CNT nanohybrid. SEM images of (b) CdS NWs, (c) CdS@Fe-PDA@ZIF-67 NWs, and (d) Fe-Co₉S₈@CNT. (e) TEM image, (f-g) HRTEM image, and (h) element mapping images of Fe-Co₉S₈@CNT.

31.0, 47.2 and 52.0° , referring to the (111), (311), (222), (511) and (440) facets of $\text{Co}_{9}\text{S}_{8}$ (PDF# 86–2273), respectively, further corroborates the formation of $\text{Co}_{9}\text{S}_{8}$. Furthermore, no obvious the characteristic peak of Fe or Fe-containing species can be detected by XRD. This finding lends further support to the hypothesis that the Fe element is likely present in the samples as clusters or single atoms. Raman spectra (Fig. S3b) employed to ascertain the degree of graphitization of the asprepared samples. The Fe-Co₉S₈@CNT possess a favorable

graphitization degree with an I_D/I_G ratio of 1.01, which can facilitate enhanced the conductivity. N_2 adsorption/desorption curves are performed to investigate the specific surface area and relevant pore size distribution (Fig. S3c and S3d). Due to the ZIF-67-derived porous structure, the Fe-Co₉S₈@CNT and Co₉S₈@CNT show a high specific surface area of 348.6 and 352.8 m^2g^{-1} , respectively, much larger than Fe@CNT (286.2 m^2g^{-1}). Furthermore, the BJH pore distribution plot demonstrates that there are rich micropores and mesopores in Fe-

 Co_9S_8 @CNT, which is beneficial to offer more space to store active S, enhance mass transfer and inhibit the volume expansion of S during operating of LSBs.

XANES and EXAFS are used to analyze the chemical state and fine structures of the Fe-Co₉S₈@CNT. Fig. 2a and FigS4a shows the Co K-edge XANES curve (Co foil, CoPc, CoS₂, Co₃O₄, CoO and Co₉S₈ as reference samples), where it can be clearly observed that the near absorption edge of Fe-Co₉S₈@CNT (the red-circled section) is positioned between that of the Co foil and CoO, indicating that the average valence state of Co in Fe- Co_9S_8 @CNT lies within the range of 0 to +2. The results are excellent agreement with the average valence state (1.78) of Co₉S₈, thereby validating the consistency and reliability of the experimental results. In addition, the Fourier transform (FT) k3-weighted EXAFS spectra (Fig. S4c) are carried out to acquire the local environment of Co center. In Fig. 2b and Fig. S4b, the reference samples Co foil, CoS2 and CoPc display obvious peaks at 2.09, 1.86 and 1.48 Å, corresponding to Co—Co bond, Co-S bond and Co-N bond, respectively. Moreover, the peak of Co—S and Co—Co bond also can be detected from 1.5 to 3.0 Å in R-space in the EXAFS spectra of Fe-Co₉S₈@CNT. However, it's worth noting the peaks of Co-Co bond in Fe-Co₂S₈@CNT increase by 0.1 Å, indicating that partial substitution of Co—Co bond with Co—Fe bond.

Then, EXAFS spectra of Fe-Co₉S₈@CNT and Co₉S₈@CNT are fitted to further understand the coordination structure of Co, the fitting

consequences (Fig. 2c, Fig. S4d and Table S2, all inappropriate R factors below 1.0 %) indicate that the Fe-Co₉S₈@CNT possesses two distinct types of Co-S coordination structures. One is Co atom connects with three S atoms (centered at 2.18 Å), and the other is Co atom coordinates with one S atom (located at 2.03 Å). Furthermore, the location of Co—Co is centered at 2.51 Å. The fitting consequences of these above-mentioned coordination structures further confirm the formation of Co₉S₈ in the sample. More importantly, the extra peak situated at 2.40 Å is attributed to the Co-Fe bond, further revealing the powerful chemical interaction between Fe and Co. The formation of the Fe—Co bond in Fe-Co₉S₈@CNT results in a reduction in the coordination number of Co-S, which is below the theoretical value, thus lead to generation of V_S in Fe-Co₉S₈@CNT. To gain further insight into the coordination environment of Co center, the wavelet transforms (WT, Fig. S4e-i) are carried out, in which the WT of Fe-Co₉S₈@CNT displays a strong signal at 5.8 \mathring{A}^{-1} , the valuable is between Co-Fe (7.6 Å^{-1}) and Co-Co (4.8 Å^{-1}), further indicating that presence of Co—Fe in the samples.

Subsequently, the Fe K-edge XANES spectra (Fig. 2d) are employed to provide further insight into the valence state and coordination structure of Fe in Fe-Co₉S₈@CNT. In Fig. 2d (the red-circled section), it can be found that the near absorption edge of Fe in Fe-Co₉S₈@CNT closely resembles that of the Fe Foil, suggesting that the valence state is near to 0. This demonstrates Fe species maybe as a metallic-like

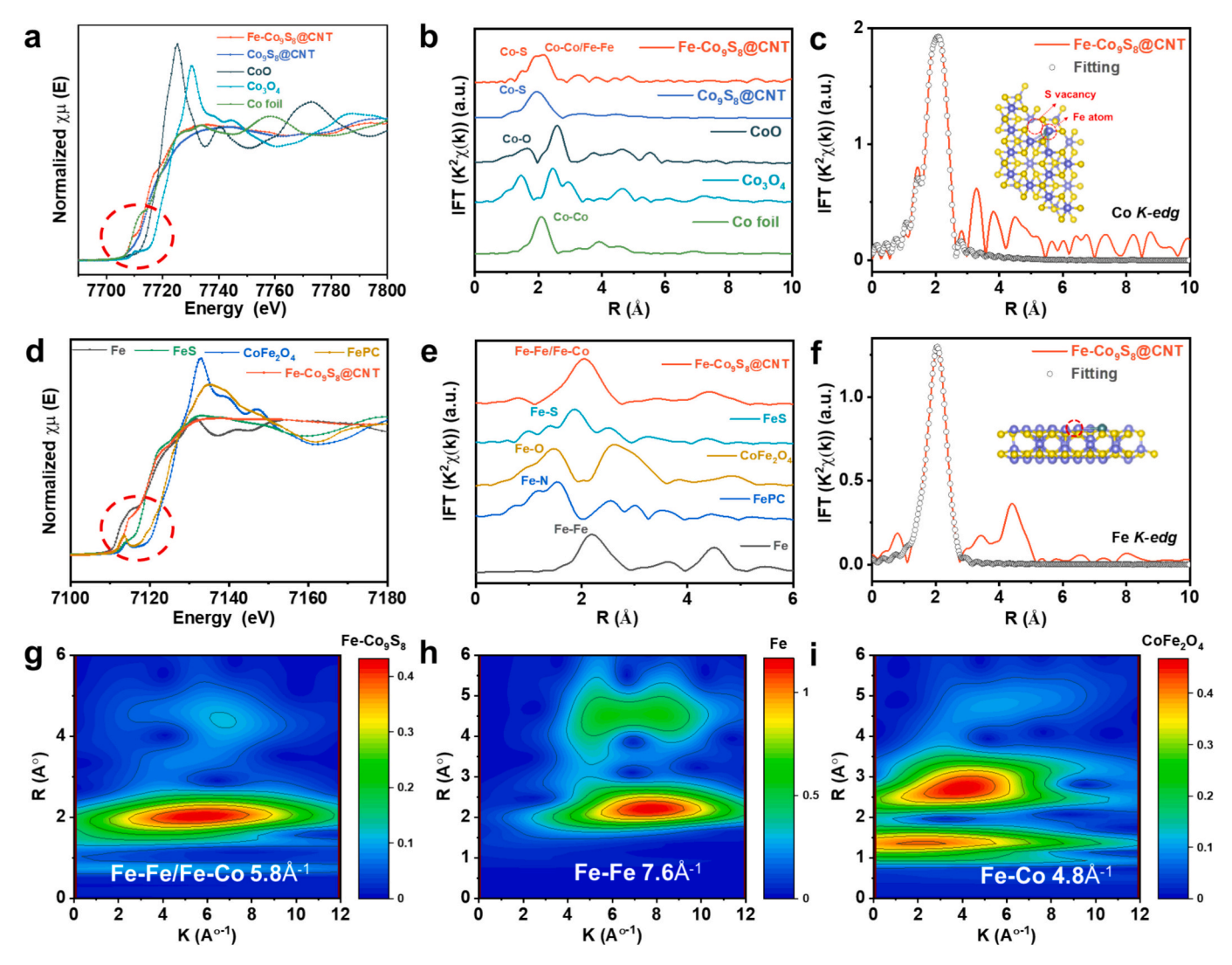


Fig. 2. (a) The Co K-edge XANES spectra and (b) Fourier transform (FT) of the Co K-edge EXAFS spectra of Fe-Co₉S₈@CNT and reference materials. (c) The Co R-space fitting results of Fe-Co₉S₈@CNT. (d) The Fe K-edge XANES spectra and (e) Fourier transform (FT) of the Fe K-edge EXAFS spectra of Fe-Co₉S₈@CNT and reference materials. (f) The Fe R-space fitting results of Fe-Co₉S₈@CNT. The wavelet transforms of (g) Fe-Co₉S₈@CNT, (h) Fe foil, and (i) CoFe₂O₄.

electronic configuration within Fe-Co₉S₈@CNT. The corresponding EXAFS spectra confirms the results, where the clear Fe-Fe bond can be observed (Fig. 2e and Fig. S5a). Moreover, no signal of Fe-S bonds can be observed, indicating that no FeSx species are produced in Fe-Co₉S₈@CNT. To further understand the coordination environment of Fe site, the EXAFS spectra are fitted, more detail can be seen in Fig. 2f, Fig. S5b and Table S2, the R factors below 1.0 % ensure the reliability of the results. Upon careful analysis, the peak located at 2.73 Å corresponds to Fe—Fe bond and the other peak at 2.43 Å ascribes to Fe—Co bond. The coordination numbers for these bonds are determined to be 0.7 and 2.2, respectively, suggesting that Fe is predominantly present in the form of Fe-Co bonds within the samples, with a minor fraction of Fe forming nanoclusters. In the WTs (Fig. 2g-i and Fig. S6), Fe-Co₉S₈@CNT expresses the highest intensity at 5.8 \mathring{A}^{-1} in k-space, which is smaller than Fe—Fe (7.6 Å^{-1}) in metallic Fe and larger than the Co—Fe (4.8 Å^{-1}) in reference CoFe₂O₄, further confirming two types of bonds in the Fe-CooSo@CNT.

XPS are performed to further estimate the surface states of the as-fabricated samples. In C1s spectrum (Fig. S7a), the peaks at 284.4, 284.8, 285.3, 286.2, and 289.0 eV can be found, attributing to C—C, C—C, C—O, C—N, and O-C=O [20,21], respectively. The formation of C—N moieties demonstrates the successful incorporation of N into the carbon skeleton. Furthermore, N1s spectrum (Fig. 3a) of Fe-Co₉S₈@CNT

could be separated into graphitic-N (400.9 eV), pyrrolic-N (399.3 eV), pyridinic-N (398.6 eV) [22,23], respectively. The pyridinic-N and pyrrolic-N can form chemical interaction with LiPSs through Li—N bond to hamper shuttle-effect. In the Co 2p profiles of Fe-Co₉S₈@CNT (Fig. 3b), the three pair of peaks (781.3/797.5 eV, 783.3/799.3 eV and 786.9 and 803.5 eV) are conformed to Co^{3+} , Co^{2+} and satellite peaks [24,25], respectively. In comparison to Co_9S_8 @CNT, the Co 2p peaks of Fe-Co₉S₈@CNT exhibit a positive shift towards higher binding energy (BE), indicating that Fe doping changes the electronic structure of Co site in Co_9S_8 to be in an electron-deficient state. The S2p spectra (Fig. 3c) further confirm the results, the BE of S2p in Fe-Co₉S₈@CNT negatively shift about 0.2 eV compared to Co_9S_8 @CNT, suggesting that S sites in Fe-Co₉S₈@CNT with rich charge density. The electron-rich S sites is beneficial to capture LiPSs by Li—S bond, whereas the electron-deficient metal sites are more readily coupled with S in LiPSs.

In order to gain further insight into the influence of Fe doping, the corresponding molecular models are built according to the characterization results to further deeply study the electron cloud distribution. As shown in Fig. 3d-e, one can find that the formation Co—Fe bonds in Co_9S_8 can induce V_S in Co_9S_8 , thereby resulting in a modification of the electron cloud density at the defect sites. In comparison to Co_9S_8 without Fe doping, a greater number of electrons are transferred from Co sites to S sites, which is in accordance with the results of XPS and XANES.

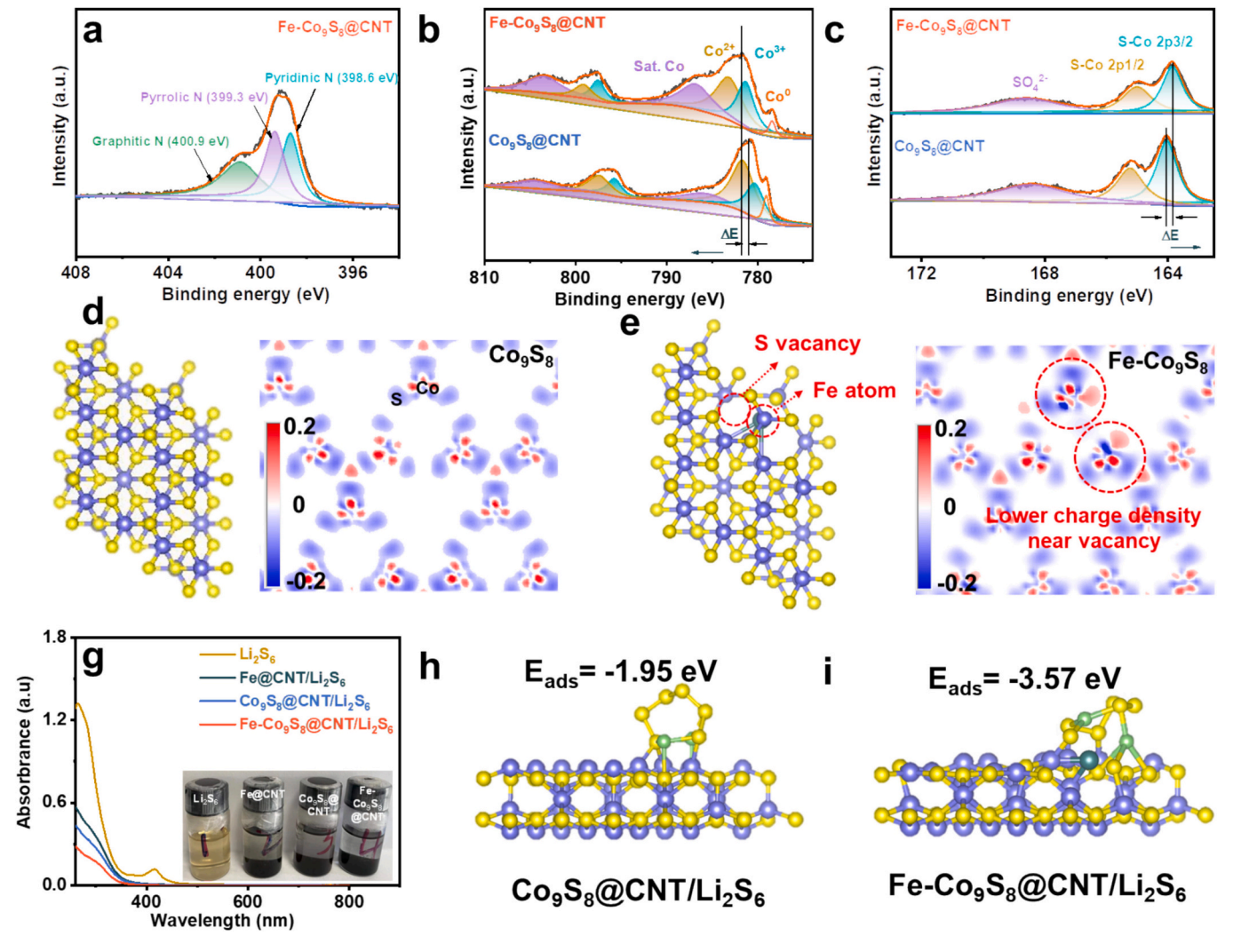


Fig. 3. (a) N1s spectra of Fe-Co₉S₈@CNT. (b) The Co2p and (c) S2p spectra of Fe-Co₉S₈@CNT and Co₉S₈@CNT. The differential charge density and relevant structural model of (c) Co₉S₈ and (d) Fe-Co₉S₈. (g) UV-vis adsorption spectra, where the insert is the relevant visualized pictures. Optimized structures and the binding energies of (h) Co₉S₈@CNT/Li₂S₆ and (i) Fe-Co₉S₈@CNT/Li₂S₆.

To analyze the LSBs performance of as-prepared samples, S/Fe-Co₉S₈@CNT, S/Co₉S₈@CNT, and S/Fe@CNT cathodes are obtained through a simple melt-diffusion process. The S loadings of different samples are quantified by thermogravimetric analysis (TGA) (Fig. S8a), which are 74.6, 74.5, and 77.8 wt% for S/Fe-Co₉S₈@CNT, S/ Co₉S₈@CNT, and S/Fe@CNT cathodes, respectively. In Fig. S8b, the corresponding XRD pattern show distinct diffraction peaks of S (PDF #42-1287). Moreover, SEM image after impregnating S (Fig. S9) demonstrates that S/Fe-Co₉S₈@CNT composite still retains 1D nanotube structure, and that no S NPs are present on the surface, suggesting that that the S is uniformly encapsulated within the hollow nanocarbon. The N2 adsorption-desorption curves and the related pore size distribution plots (Fig. S10) provide further confirmation that the S has successfully infiltrated the pore and channel structures. It can be observed that the specific surface area and corresponding pore volume decline significantly after S loading.

The static adsorption measurements are further conducted to estimate the affinity of as-prepared samples towards LiPSs. In Fig. 3g inset, the color of solution for the Fe-Co₉S₈@CNT-Li₂S₆/THF changes to nearly clear after sufficient interaction, while the Li₂S₆/THF solution with Co₉S₈@CNT or Fe@CNT additives still maintains pale-yellow, which suggests that Fe doping can markedly enhance the absorptive capacity of Co₉S₈ for LiPSs. This result is corroborated by the UV–vis spectra (Fig. 3g), where Fe-Co₉S₈@CNT exhibits the smallest Li₂S₆-relevant absorbance peaks, in comparison to the other samples. To further verify the excellent adsorption capacity towards LiPSs, the adsorption energies of different samples are evaluated according to DFT calculation, corresponding model in Fig. S11–12. As depicted in Fig. 3h-i, the Fe-Co₉S₈@CNT shows a lower adsorption energy (–3.57 eV) towards to Li₂S₆ than that of Co₉S₈@CNT (–1.94 eV), demonstrating that the Li₂S₆ more easily anchored on the Fe-Co₉S₈@CNT surface.

To further explain the reason, the surface chemical state of Fe-Co₉S₈@CNT after adsorbing Li₂S₆ are also estimated by XPS measurement. Fig. S13a-b show that the BE of Co2p and Fe 2p in Fe-Co₉S₈@CNT occur different blue shift compared with initial, demonstrating the existence of powerful chemical interactions between LiPSs and metal sites. The S2p spectrum (Fig. S13c) exhibits the obvious terminal sulfur (S_T^{-1} , 165.4 eV) and bridge sulfur (S_B, 164.0 eV), which are corresponded to the presence of Li₂S₆ [26,27]. Compared with pure Li₂S₆, the binding energies of terminal sulfur and bridge sulfur of Fe-Co₉S₈@CNT both move in a positive direction, demonstrating that there is a chemical interaction between Fe-C₀₉S₈@CNT and Li₂S₆. Due to catalysis of Fe-Co_oS₈@CNT, a new peak (169.6 eV) of thiosulfate/polythionate derived from Li₂S₆ can be observed [28]. The appearance of this salt is beneficial to the forms of solid Li₂S with remarkable electrochemical activity and regeneration during the charging/discharging process. In Li1s spectrum (Fig. S13d), three peaks located at 56.8, 55.6, and 54.5 eV can be observed, assigning to Li-N, Li-O, and Li-S bond [29,30], respectively, the appearance of Li-N/Li-O further confirming the strong interaction between Fe-Co₉S₈@CNT and LiPSs, therefore remarkably hampering the "shuttle effect" and establishing the basis of further transformation of LiPSs.

In addition to adsorption, diffusion and charge transfer also play a significant role in complex battery reactions in S cathodes. Electrochemical measurements are performed to further proof the superiorities of Fe-Co₉S₈@CNT in terms of S involved redox kinetics and masstransfer procedure. The diffusivity procedure is estimated through Cyclic voltammetry (CV) measurements with different scan rates of 0.1–0.5 mV s⁻¹, as depicted in Fig. S14, in which the redox peaks potential gaps and redox peak currents are increased with the increasing scanning rate. Compared to other as-fabricated cathodes, S/Fe-Co₉S₈@CNT cathode delivers the highest peak currents and smallest potential gaps (11, 45 and 32 mV), which suggests that Fe-Co₉S₈@CNT has the optimal kinetic and catalytic activity. Furthermore, in both the oxidation and reduction procedures, the peak current densities of asprepared sulfur cathodes are proportional to the square root of the

scan rates (Fig. S15a-c), suggesting that the diffusion is the rate-limiting step in the entire electrochemical reaction. According to the Randles–Sevcik equation (Eq. S1), the slope represents the acceleration of mass-transfer procedure on the surface. Furthermore, the calculated Li $^{\rm +}$ diffusivity coefficient of the as-prepared cathodes based on Eq. S1 are depicted in Fig. S14d. Obviously, the S/Fe-Co₉S₈@CNT cathode possesses the fastest Li $^{\rm +}$ diffusivity and best reaction kinetics than other prepared cathodes during cell reaction procedures.

In order to further evaluate the effect of Fe-Co₉S₈@CNT on the kinetics of S cathode, the galvanostatic intermittent titration techniques (GITT) are performed at 0.1C. The S/Fe-Co₉S₈@CNT cathode indicates the best Coulomb efficiency (95.0 %) and discharge capacity (1383.4 mAh g $^{-1}$) than other as-prepared cathodes (Fig. S16). Furthermore, the corresponding internal reaction resistances were estimated according to the following equation:

$$\Delta R_{internal} = |\Delta V_{QOCV-CCV}| / I_{applied} \tag{1}$$

where the ΔV is voltage gap between the quasi-open circuit and the closed voltage, and I $_{applied}$ represents current applied. The ΔR $_{internal}$ is the internal resistance of the as-prepared cathodes attributing to normalization time of the discharge/charge processes. Significantly, the S/Fe-Co₉S₈@CNT cathode delivers the lowest ΔR $_{internal}$ during discharge/charge stages compared to Co₉S₈@CNT and Fe@CNT cathode (Fig. S17), further implying that Fe-Co₉S₈@CNT can efficiently reduce the reaction kinetics of the S reaction.

To deeply understand the electrocatalytic activity towards the transformation of LiPSs of Fe-Co₉S₈@CNT, the Li₂S₆ symmetric cells are performed. In CV profiles of as-prepared symmetric cells (Fig. 4a), Fe-Co₉S₈@CNT shows two obvious pairs of redox peaks could be discovered at -0.133/-0.004 and -0.001/0.123 V, corresponding to the multistep LiPSs transformation reactions [31]. For comparison, Co₉S₈@CNT and Fe@CNT exhibit the larger potential hysteresis with two wider redox peaks, which proves that Fe-Co₉S₈@CNT has higher reaction kinetics and activity for LiPSs transformation than Co₉S₈@CNT and Fe@CNT. Moreover, Fe-Co₉S₈@CNT symmetric cells also display the largest peak area in the CV curves, confirming its outstanding S utilization. In Fig. S18, EIS posts show that the Fe-Co₉S₈@CNT symmetric cells display the low charge transfer resistance (R_{ct}) that of only 21.3 Ω , better than Co₉S₈@CNT (52.1 Ω) and Fe@CNT (70.5 Ω), further indicating remarkable sulfur redox kinetics of Fe-Co₉S₈@CNT.

Chronoamperometry measurements with Li₂S₈/TEG solution as active material are conducted to investigate the nucleation/dissolution kinetics of Li₂S. As presented in Fig. 4b, the monotonically decreasing initial current corresponds to the transformation from Li₂S₈ to Li₂S₄, and following current peak is attributed to the further precipitation and growth of solid Li₂S. Compared to others, Fe-Co₉S₈@CNT electrode expresses the sharpest precipitation peak (Ip = 0.036 mA) and earliest precipitation time (t = 6674 s), suggesting rapid precipitation of solid Li₂S. In general, the nucleation capacity is related to the integrated area under the current profiles. Compared to Co₉S₈@CNT (194.5 mAh g⁻¹) and Fe@CNT (148.8 mAh g⁻¹) electrodes, the Fe-Co₉S₈@CNT electrode displays the highest specific capacity of 225.3 mAh g⁻¹, illustrating the Fe-Co₉S₈@CNT possess remarkable nucleation capacity of Li₂S. The SEM images after the deposition of Li₂S (Fig. S19a-c) indicat that Fe-Co₉S₈@CNT electrode could induce the 3D uniform deposition and the following growth of insoluble Li₂S precipitates, thus avoiding their blocky growth and accumulation. To further obtain the insights into Li₂S nucleation morphologies on distinct surface, the dimensionless diagnostic analysis of the i-t profiles obtained through Li₂S nucleation measurements is conducted based on the Scharifker-Hills models [32], as shown in Fig. 4c-e. Nucleation is divided into progressive nucleation (P) and transient nucleation (I). Growth is divided into attachment atoms binding to the lattice interface (2D) and volumetric diffusioncontrolled growth (3D) [33]. The growth and nucleation of Li₂S are controlled by the 3DI, 3DP, 2DI, and 2DP deposition patterns. The

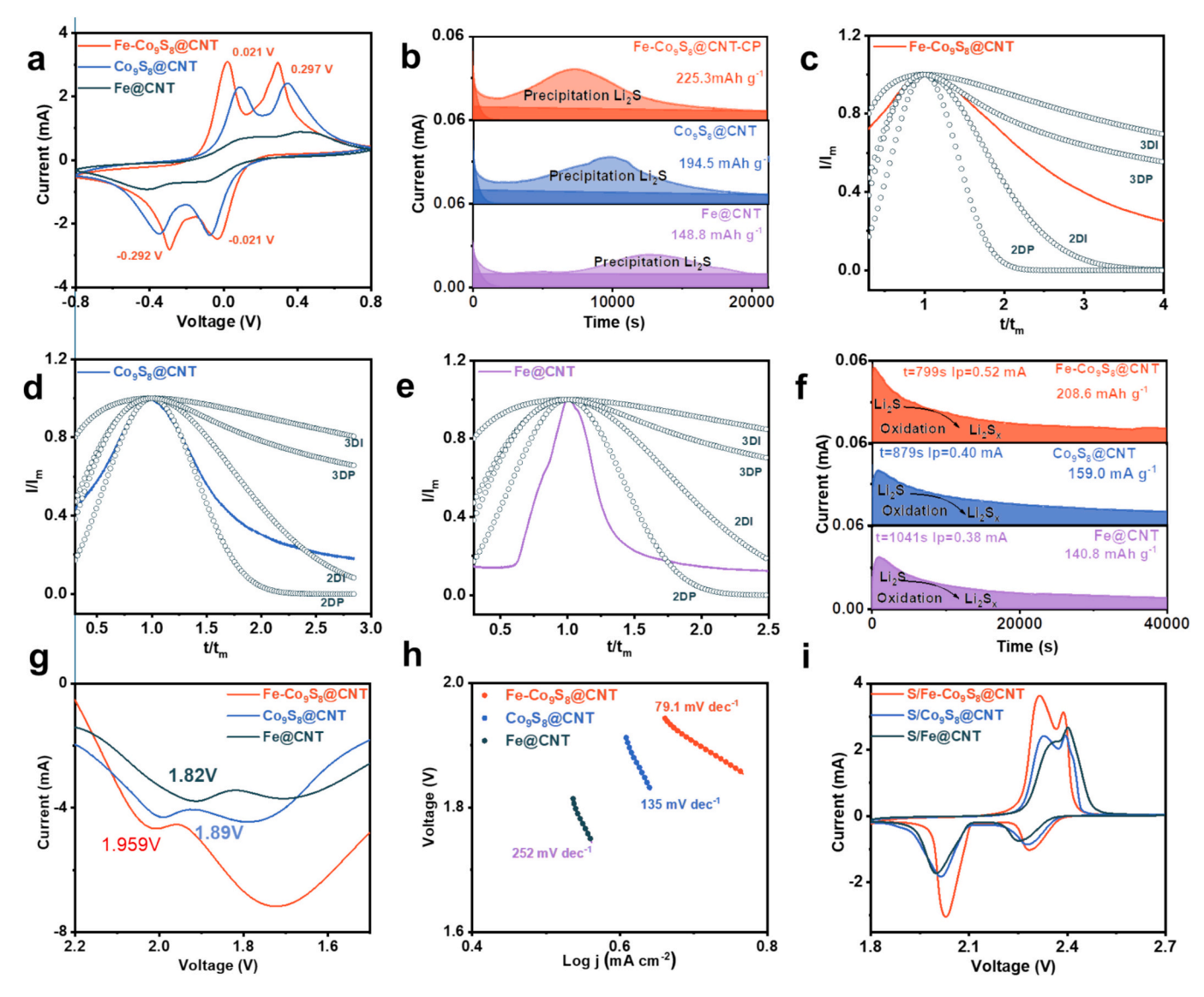


Fig. 4. (a) CV profiles of three symmetrical cells. (b) Potentiostatic discharge, (c-e) appropriate dimensionless i-t transients, and (f) potentiostatic charge curves of three electrodes. (g) LSV curves and (h) the relevant Tafel slopes of different electrodes. (i) CV curves of different cathodes.

transient profiles are classified via the nucleation/growth area (t/t_m<1) $\,$ and growth governing area ($t/t_m > 1$). The Li₂S nucleation behavior is schematically illustrated in Fig. S20. In view of the Fe@CNT electrode, nucleation is hindered because of the lack of electroactive sites. Therefore, Li₂S grows unevenly at a limited nucleation site, leading to insufficient S utilization. On the other hand, the precipitation of the Fe-Co₉S₈@CNT electrode is mainly controlled by 2DI, demonstrating that Li₂S is uniformly nucleated and grows faster along the surface under the rapid reduction reaction [34]. In the growth area ($t/t_m > 1$), 2DI and 3DP growth models are hybridized in the Fe-Co₉S₈@CNT electrode, thus maximizing Li₂S transformation. The Co₉S₈@CNT electrode shows the high 2D model ratio consisted of mostly progressive nucleation, suggesting uneven Li₂S precipitation and growth on the Co₉S₈@CNT surface. Fig. 4f exhibits the Li₂S dissolution procedures, similar to nucleation, the Fe-Co₉S₈@CNT electrode delivers a highest dissolution current response (Ip = 0.52 mA), earliest dissolution time (799 s), and best dissolution capacity (208.6 mAh g⁻¹) compared to Co₉S₈@CNT (0.40 mA, 879 s, 159.0 mAh $\rm g^{-1}$) and Fe@CNT (0.38 mA, 1041 s, 140.8 mAh g⁻¹). These above results confirm Fe-Co₉S₈@CNT exhibits the outstanding S bidirectional catalytic activity.

The electrocatalytic activity of Fe-Co₉S₈@CNT towards the LiPSs

conversion is also evaluated via Linear sweep voltammetry (LSV). In Fig. 4g, Fe-Co₉S₈@CNT, Co₉S₈@CNT, and Fe@CNT electrodes display the current peaks located at 1.959, 1.89 and 1.82 V, respectively, which represents the liquid LiPSs to solid Li₂S₂/Li₂S phase transition [35]. Significantly, compared with others, the Fe-Co₉S₈@CNT electrode indicates the highest peak intensity and voltage, which demonstrates a rapid phase transition on that surface. Meantime, the Fe-Co₉S₈@CNT electrode displays the smallest Tafel plots of 79.1 mV dec⁻¹ compared with other electrodes (Fig. 4h), further confirming improved reaction kinetics of the Fe-Co₉S₈@CNT.

The CV curves (Fig. 4i) of the as-fabricated cathodes indicate two evident reduction peaks, attributed to conversion from S to the high-order LipSs (Li₂S_x, $4 \le x \le 8$) and then reduction to insoluble Li₂S₂/Li₂S, respectively. Meanwhile, the two oxidation peaks are ascribed to oxidation from Li₂S₂/Li₂S to the soluble LiPSs, and further transformation to S [28]. Compare with S/Co₉S₈@CNT (Ip = 1.72 mA) and S/Fe@CNT (Ip = 1.83 mA) cathodes, S/Fe-Co₉S₈@CNT cathode displays the highest reduction current peak (Ip = 3.05 mA) at about 2.04 V, demonstrating the transformation of soluble LiPSs to insoluble Li₂S₂/Li₂S much easier to carry out with Fe-Co₉S₈@CNT. Moreover, the voltage gap of S/Fe-Co₉S₈@CNT cathode between the reduction current

peaks and oxidation current peak is only 105 and 273 mV, far superior to S/Co₉S₈@CNT (151 and 315 mV) and S/Fe@CNT (160 and 359 mV) cathodes, further suggesting excellent S bidirectional catalytic activity of Fe-Co₉S₈@CNT.

The second galvanostatic charge-discharge profiles (GCD) at 0.1C of the as-prepared cathodes (Fig. 5a-b) show that the S/Fe-Co₉S₈@CNT cathode possesses a low interfacial energy barrier of only 24 mV, smaller than that S/Co₉S₈@CNT and S/Fe@CNT cathodes (34 and 39 mV). Additionally, the onset potential for the S/Fe-Co₉S₈@CNT cathode is only 1.974 V compared to S/Co₉S₈@CNT (2.154 V) and S/Fe@CNT (2.179 V) cathodes, which suggests that Fe-Co₉S₈@CNT can meliorate discharging behavior. Meantime, the obviously reduced charging potential obstacle of the S/Fe-Co₉S₈@CNT cathode (2.21 V) also discloses the remarkable Li₂S decomposition kinetics of Fe-Co₉S₈@CNT. More important, the S/Fe-Co₉S₈@CNT cathode possesses the lowest polarization value that of only 128 mV compared to S/Co₉S₈@CNT and S/ Fe@CNT cathodes (148 and 191 mV), which illustrates a reduced voltage hysteresis. These results indicate the lower kinetic barrier for the LiPSs transformation on the Fe-Co₉S₈@CNT surface. From the GCD profiles, the discharge profile shows two apparent plateaus, where Q1 assigns to solid-liquid transformation procedure of S to Li₂S₄, while Q2 attributes to liquid-solid transformation procedure of Li_2S_4 to Li_2S_2 /Li₂S. The activation overvoltage of Li₂S for S/Fe-Co₉S₈@CNT cathode is only 2.21 V during the second charging, much smaller than S/

 $\text{Co}_9S_8@\text{CNT}$ (2.218 V) and S/Fe@CNT (2.236 V) cathodes. In addition, the ratios of Q2 to Q1 for S/Fe-Co $_9S_8@\text{CNT}$, S/Co $_9S_8@\text{CNT}$ and S/Fe@CNT cathodes are estimated to be 2.67, 2.22and 2.11 (**Table S3**), respectively, illustrating that Fe-Co $_9S_8@\text{CNT}$ can significantly promote LiPSs conversion.

In situ Raman spectroscopy is then performed to analyze the adsorption and catalytic capacity towards LiPSs of Fe-Co₉S₈@CNT, the test device is shown in Fig. 5c, where LiPSs could be qualitatively tested in real time via the quartz observation window. In Fig. 5d and S21a, one can find that there are no obvious signals of LiPSs (Li₂S₈, Li₂S₄ and Li₂S₆) in the Raman spectra of S/Fe-Co₉S₈@CNT cathode during the discharge and charge process under different potential [36,37]. In contrast experiment, Raman spectra (Fig. 5e and S21b) of the S/C cathode exhibits clear peaks at 161.7, 463.3 and 491.0 cm⁻¹ during charge and discharge process, which are assigned to the features peaks of Li₂S₈, Li₂S₄ and Li₂S₆ [38,39], respectively. The results further suggest that Fe-Co₉S₈@CNT expresses superior ability to adsorption and bidirectional catalysis of LiPSs, which effectively inhibits the dissolution and shuttling of LiPSs.

DFT calculations are further employed to deeply investigate the catalytic mechanism of Fe-Co₉S₈@CNT for LiPSs conversion. Fast electron transfer is a key to enhancing of LiPSs redox and electrochemical property. To this end, density of states (DOS) of Fe-Co₉S₈ and Co₉S₈ are estimated by theoretical calculation in Fig. S22, in which the bandgap of

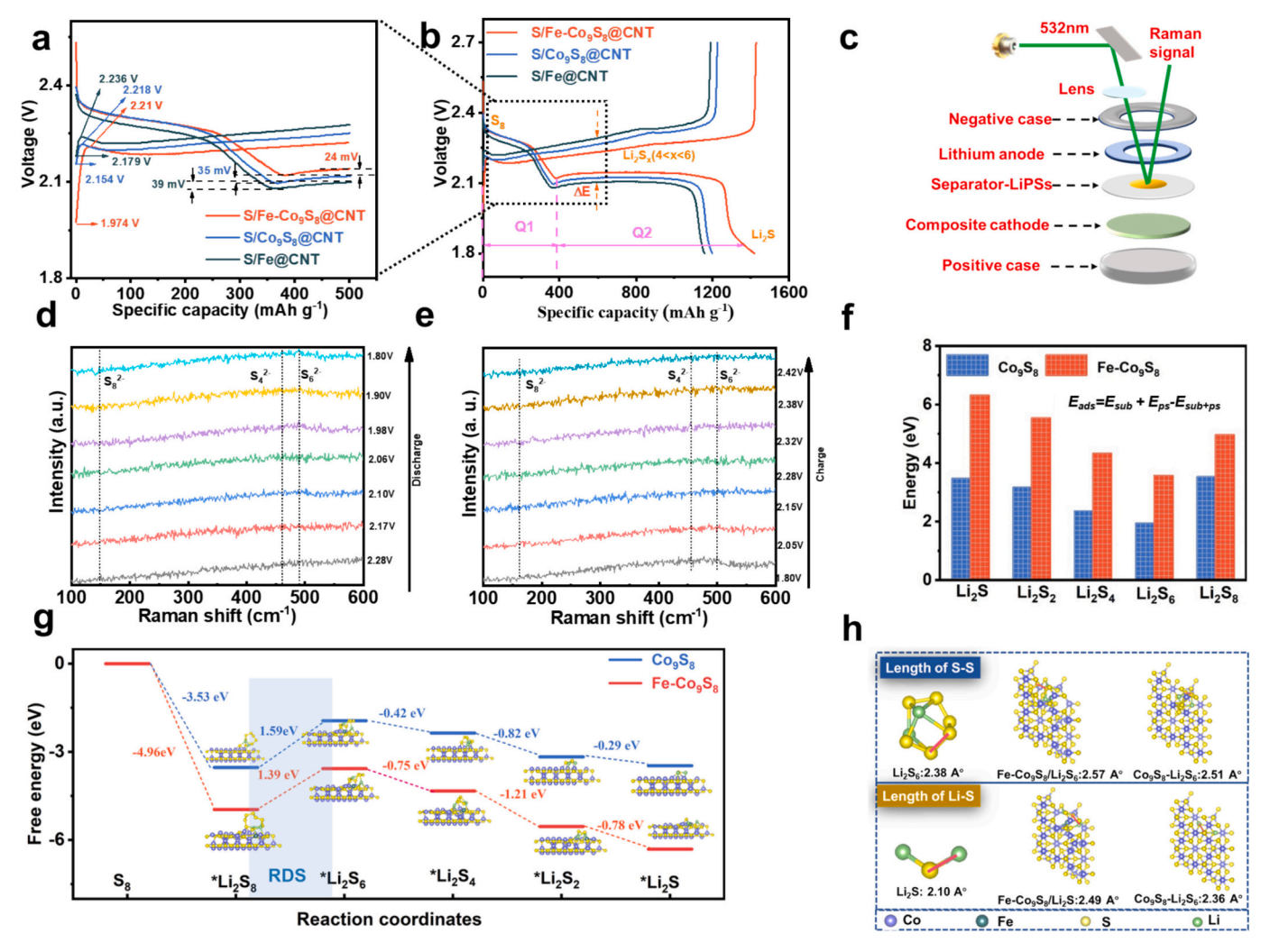


Fig. 5. (a-b) GCD curves at 0.1C of different cathodes. (c) Schematic of in situ Raman measurements. (d-e) The selected original Raman spectroscopy of S/Fe-Co₉S₈@CNT and S/C cathodes during discharge processes. (f) The binding energies between Li₂S_x (x = 0, 2, 4, 6, 8) and catalysts. (g) Gibbs free energy of Li₂S_x (x = 0, 2, 4, 6, 8) on the catalyst during sulfur transformation reaction. (h) the S—S bridged bond of Li₂S₆ and Li—S bond of Li₂S on the surface of catalysts.

Fe-Co₉S₈ is only 0.015 eV, smaller than that of Co₉S₈ (0.095 eV), suggesting that Fe doping can reduce the bandgap of Co₉S₈, make the valence band closer to the Fermi level, which can enhance the metallic features of Co₉S₈ to promote electron transfer and improve catalytic performance during electrochemical reaction. Fig. 5f shows the binding energies between Li₂S_x (x = 0, 2, 4, 6, 8) and different samples, benefit from synergies with V_S and metal sites in Co₉S₈, the adsorption behavior of Li₂S_x (x = 0, 2, 4, 6, 8) on Fe-Co₉S₈ are better than those on the Co₉S₈. Fig. 5g shows the Gibbs free energy changes (Δ G) of different steps in S electrochemical reduction on surface of Fe-Co₉S₈ and Co₉S₈, in which the S transformation is a multi-step electrochemical reaction, and the RDS is the transformation between Li₂S₈ and Li₂S₆. The Δ G (1.39 eV) of the RDS on surface of Fe-Co₉S₈ is smaller than that of Co₉S₈ (1.59 eV), indicating the thermodynamically profitable S reduction on the surface

of Fe-Co₉S₈. Moreover, in Fig. 5h, one can find that the Fe-Co₉S₈ expresses the much longest S—S bridged (2.57 Å) and Li—S (2.49 Å) bonds than those of Co₉S₈ and pristine Li₂S₈/Li₂S, revealing that the Fe-Co₉S₈ can significantly weaken the S—S bridged and Li—S bond, thus facilitating the bidirectional conversion of LiPSs.

Moreover, the spin-states of Fe-Co₉S₈ and Co₉S₈ are further considered, as depicted in Fig. 6. Electron paramagnetic resonance (EPR) experiments (Fig. S23a) are firstly performed to investigate the unpaired electrons on Co actives in Fe-Co₉S₈@CNT and Co₉S₈@CNT, where Fe-Co₉S₈@CNT exhibits the higher peak intensity compared with Co₉S₈@CNT, demonstrating the increased unpaired electrons in Fe-Co₉S₈@CNT, which is attributed to the d-orbital electron configuration conversion partial Co actives. The d-orbital electron configuration of Co active sites in Fe-Co₉S₈@CNT is further evaluated through temperature-

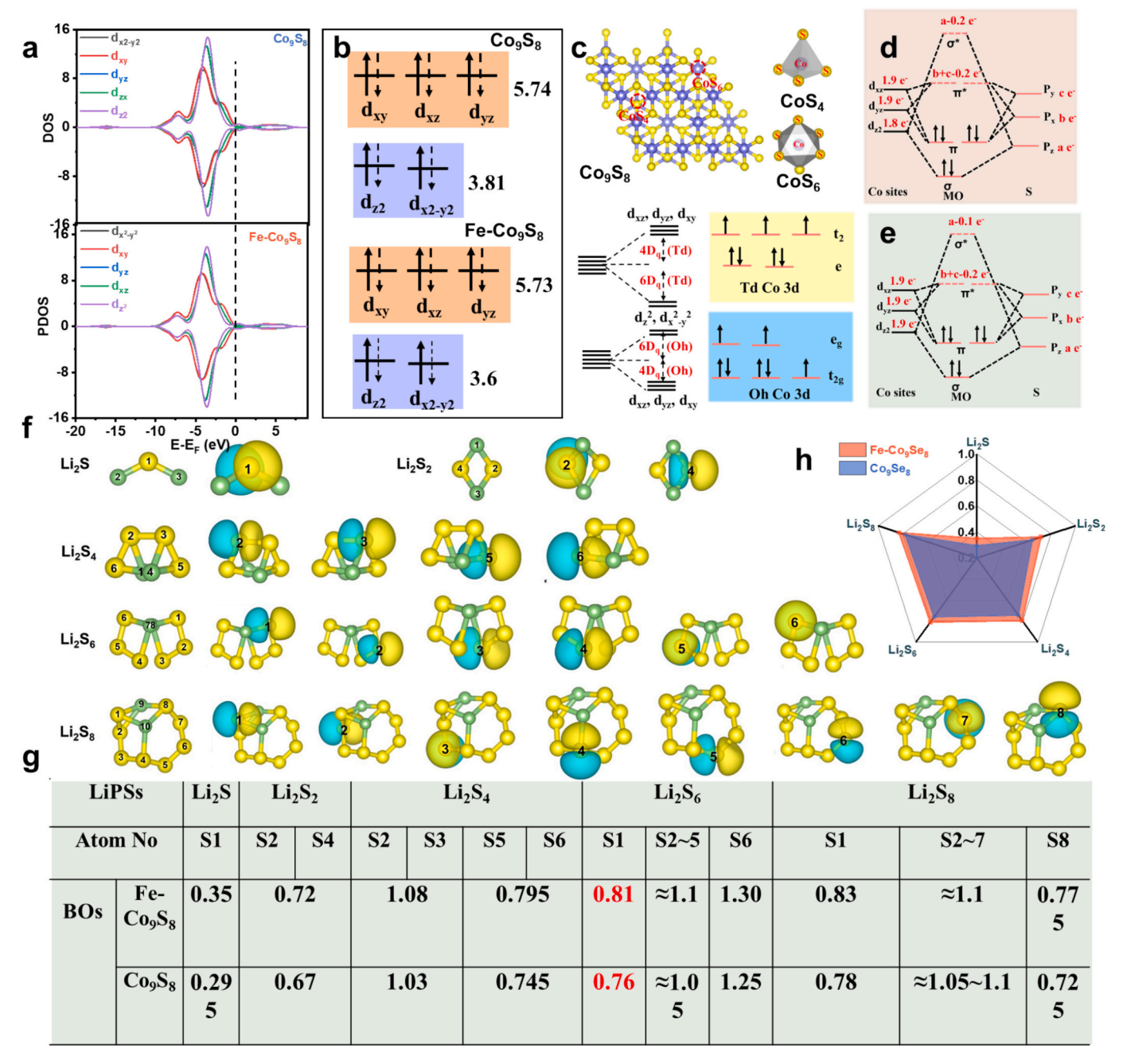


Fig. 6. (a) The PDOS profiles, (b) the Co 3d orbit occupancies of Fe-Co₉S₈@CNT and Co₉S₈@CNT. (c) The Co₉S₈ lattice structure and the Td/Oh spin configurations. (d-e) The MO of Co sites of Fe-Co₉S₈ and Co₉S₈ coupled with S of Li₂S_x. (f) The atomic configuration of Li₂S_x. (g-h) The BOs of Fe-Co₉S₈ and Co₉S₈ between different Li₂S_x.

dependent magnetization (M-T) experiments (Fig. S23b). The susceptibility of the materials follows a paramagnetic Curie-Weiss law: $\chi=C/(T-\Theta)$ when the temperature is above 50 K, where C represents the Curie constant and Θ represents the Curie-Weiss temperature [16]. According to the fitting results, the effective magnetic moment (μ_{eff}) of FeCo₉S₈@CNT and Co₉S₈@CNT are calculated to be 5.00 and 4.89 μ_B , respectively (Fig. S23c). The μ_{eff} of transition metal's 3d orbital is often derived from the spin splitting of its partially occupied d orbitals (eg and t_{2g}). Therefore, Fe-Co₉S₈@CNT indicates the higher spin state stems from the d orbitals electronic redistribution.

Furthermore, DFT computations are further conducted to investigate the electronic occupancy of d orbitals in Fe-doping optimized Co₉S₈. The PDOS profiles first reveal the obvious alteration of the spin configuration after the formation of Fe-Co₉S₈ compared with Co₉S₈ (Fig. 6a). In general, Co₉S₈ has more complete occupancy states below the Fermi level (E_F) compared to Fe-Co₉S₈, as demonstrated via the high PDOS under E_F. Based on the PDOS profiles, the dz^2 and dx^2-y^2 (the two orbits are defined as eg orbits) occupancies are smaller in Fe-Co₉S₈ than in Co₉S₈. Specifically, the occupancy of the e_g orbit is 3.81 for Co₉S₈ while the Fe-Co₉S₈ indicates is 3.60, as presented in Fig. 6b. Furthermore, the occupancy of $d_{xz}+d_{xy}+d_{yz}$ orbits (t₂ orbit) are 5.74 and 5.73 for Co₉S₈ and Fe-Co₉S₈, respectively, which are typically the same. Therefore, the major differences in spin configurations of Co₉S₈ and Fe-Co₉S₈ lies in the occupancy of e_g orbit. Furthermore, the occupancies of t_{2g} orbitals are both about 5.8 e⁻ in Fe-Co₉S₈ and Co₉S₈, which are significantly higher than a conventional four-coordinated high-spin Co and should originate from the six-coordinated Co sites in the lattice (Fig. 6c). In a typical tetrahedral field (O_{Td}), the five-degenerate d orbitals could be split into t_{2g} orbitals with higher energy $(d_{xz}, d_{xy}, \text{ and } d_{yz})$ and e orbitals (dz^2) and dx^2-y^2) with lower energies [40]. Subsequently, the electrons in 3d orbits will fill the orbital based on the relative energy between pairing energy (P) and splitting energy (Δ_0) [41]. Typically, owing to the higher energy barrier of t_{2g} orbits, the largest t_{2g} orbits occupancy (d_{xz} , d_{xy} , and d_{yz}) is 3 for Co²⁺ with 7 electrons in 3d orbits (Fig. 6c). The much larger t_{2g} orbits filling (ca. 5.73) origins from the CoO_6 octahedral (Oh) structures in the Co₉S₈ lattice, in which the d_{xz} , d_{xy} , and d_{yz} orbits are the smaller-energy orbits (t2g) and therefore the maximum occupancies of d_{xz} , d_{xy} , and d_{yz} orbits could achieve to 6 in the Oh lattice.

Generally, LiPSs and Li₂S are the main intermediates of the LSB system, and their effective electronic states depend on the 3p orbital of sulfur. Because of the restriction of symmetry, the S 3p₂-orbital would strongly interact with the $3dz^2$ -orbital, developing the σ and σ^* bonds, while $3p_v$ and $3p_v$ would develop the π and π^* bonds with $3d_{vz}$ and $3d_{vz}$. respectively [42,43]. Therefore, the adsorption capabilities for the LiPSs between Fe-Co₉S₈ are further estimated through the bond orders (BO) as following: BO = $(n_{\text{bonding}} - n_{\text{anti-bonding}})/2$. Hence, n_{bonding} and $n_{\text{anti-bonding}}$ are the number of electrons bonding orbitals and anti-bonding orbitals, respectively. The larger the BO means the stronger adsorption ability. Besides, due to t_{2g} orbital occupancies are same for Fe-Co₉S₈ and Co₉S₈, with around 5.7 e^- in t₂ orbital based on the DFT calculation, the d_{xz} and d_{yz} occupancies are 1.9 e^- for both Fe-Co₉S₈ and Co₉S₈. Additionally, the dz^2 occupancies of Fe-Co₉S₈ and Co₉S₈ are 1.8 and 1.9 e^- , respectively. The p_z , p_x , and p_y are defined as a, b, and c (0 \leq a, b, and c \leq 2). Therefore, the molecular orbits between the Co sites and S of Li_2S_x (x = 0, 2, 4, 6 and 8) are deduced, as shown in Fig. 6d-e The BO for Fe-Co₉S₈ and Co₉S₈ are then estimated as following:

$$\begin{split} \text{Fe} - \text{Co}_9 S_8 : & \text{BO}_{\text{Co}^*S} = \left[6 - (a - 0.2) - (b + c - 0.2)\,\right] / 2 \\ & = \left[6.4 - (a + b + c)\,\right] / 2 = 3.2 - (a + b + c) / 2 \end{split}$$

$$\begin{split} \text{Co}_9 S_8 : & BO_{\text{Co*S}} = [6 - (a - 0.1) - (b + c - 0.2)\,]/2 = [6.3 - (a + b + c)\,]/2 \\ & = 3.15 - (a + b + c)/2 \end{split}$$

Impressively, the NBO first analyzes the electronic structure configuration of LiPSs during the whole sulfur conversion reaction as shown in

Fig. 6f and Table S4–8. Therefore, all BOs of Fe-Co₉S₈ are larger compared to Co₉S₈, as depicted in Fig. 6g-h, demonstrating a strong adsorption capability and agree with the DFT results. In summary, based on the above investigations according to molecular orbit and spin-tronics, the Fe doping into Co₉S₈ can improve the adsorption capability of the Co sites and therefore further can effectively promote the LiPSs conversion through reduce the ΔG of the rate-determining step.

Based on excellent sulfur carrying, adsorption and catalytic capabilities, S/Fe-Co₉S₈@CNT cathode displays a favorable rate capability and cycle stability. Fig. S23d illustrates the initial discharge capacity of the S/Fe-Co₉S₈@CNT cathode, which exhibits an exceptional 1401.3 $mAh g^{-1}$ at 0.1 C with a remarkable Coulombic efficiency of 99.2 %, and can maintains a discharge capacity of 1323.9 mAh g⁻¹ after cycling for 100 cycles, significantly outperforming the those of S/Co₉S₈@CNT $(1222.5 \text{ and } 1060 \text{ mAh g}^{-1})$ and S/Fe@CNT cathodes $(1039.1 \text{ and } 785.2 \text{ m}^{-1})$ $mAh g^{-1}$). Following, the rate performance tests between 0.1 C and 5.0 C (Fig. 7a) indicates the S/Fe-Co₉S₈@CNT cathode exhibits highest discharge capacities of 1465.1, 1386.4, 1212.2, 1086.5, 950.2, 843.5, and 775.7 mAh g^{-1} at 0.1, 0.2, 0.5, 1.0, 2.0, 3.0, and 5.0 C respectively. In case of the rate density returns to 0.2 C, it remains displays a superior discharge capacity 1371.3 mAh g⁻¹, demonstrating the remarkable durability and stability during cycling at different discharge current rates. For comparison, the S/Co₉S₈@CNT and S/Fe@CNT cathodes express inferior rate performance, particularly when the current rate increases to 5.0C, only 489.2 and 400.9 mAh g⁻¹ can be maintained, respectively. Besides, the corresponding GCD curves at various current densities of the S/Fe-Co₉S₈@CNT cathode maintains the one typical charge voltage plateau and two discharge voltage plateaus (Fig. S24a-c), and Fig. S24d shows the polarization values at different rates of three cathodes, where S/Fe-Co₉S₈@CNT cathode displays smallest polarization values than those of others, further demonstrating the superiority of S/Fe-Co₉S₈@CNT cathode.

The long cycling stable property is a significant standard for the application of LSBs. As shown in Fig. 7b and Fig. S27, the S/Fe-Co₉S₈@CNT cathode demonstrates an outstanding specific capacity preservation of 1039.1 mAh g⁻¹ over 500 cycles with a decay of only 0.01 % each cycle at 1.0 C, far superior to S/Co₉S₈@CNT cathode (679.8 mAh g^{-1} and 0.06 %) and S/Fe@CNT cathode (594.0 mAh g^{-1} and 0.07 %). When the current rate rises to 3.0C, the S/Fe-Co₉S₈@CNT cathode still delivers a favorable initial specific capacity of 899.1 mAh g⁻¹ and achieves outstanding capacity retention of 87.8 % over 1000 cycles, assigning to an ultralow capacity attention of 0.022 % each cycle (Fig. 7c). Impressively, the Coulombic efficiencies of S/Fe-Co_oS₈@CNT cathode at 1.0/3.0C both are close to 100 %, further suggesting that Fe-Co₉S₈@CNT effectively promotes the redox reaction in LSBs. Moreover, the SEM images of Li anodes of three cathodes post-cycle at 1.0C over 500 cycles (Fig. S25) show that Li anode of S/Fe-Co₉S₈@CNT cathode delivers the smooth and sleek surface, but apparent lithium dendrite can be found of other cathodes, further indicating that Fe-Co₉S₈@CNT can effectively restrict the shuttle effect of LiPSs to confine the growth of Li dendrites. In the Nyquist plots before and after cycle (Fig. S26), the precycle EIS curve exhibits a slash in the low frequency area and one semicircle in the high frequency area, which is attributed to Warburg dispersion impedance (Wo) and the charge transfer resistance (Rct), respectively. After 500 cycles, a fresh semicircle appears on the middle frequency area, corresponding to solid layer accrued resistance (Rs). Apparently, the S/Fe-Co₉S₈@CNT cathode exhibits the considerably lowest resistances both in before and after cycle, demonstrating that the Fe-Co₉S₈@CNT can facilitate the electron transfer kinetics. In addition, the W_{o} and R_{ct} of post-cycle cathodes are smaller compared with fresh cathodes, corresponding to the electrolyte gradually impregnating into the cathode and the re-distribution of active sulfur on the cathode

Implementing high S utilization rate and steady cycle under harsh condition (S loading >4 mg cm $^{-2}$, E/S < 10 μL mg $^{-1}$) is important for application of LSBs with high-energy density, but still faces challenges.

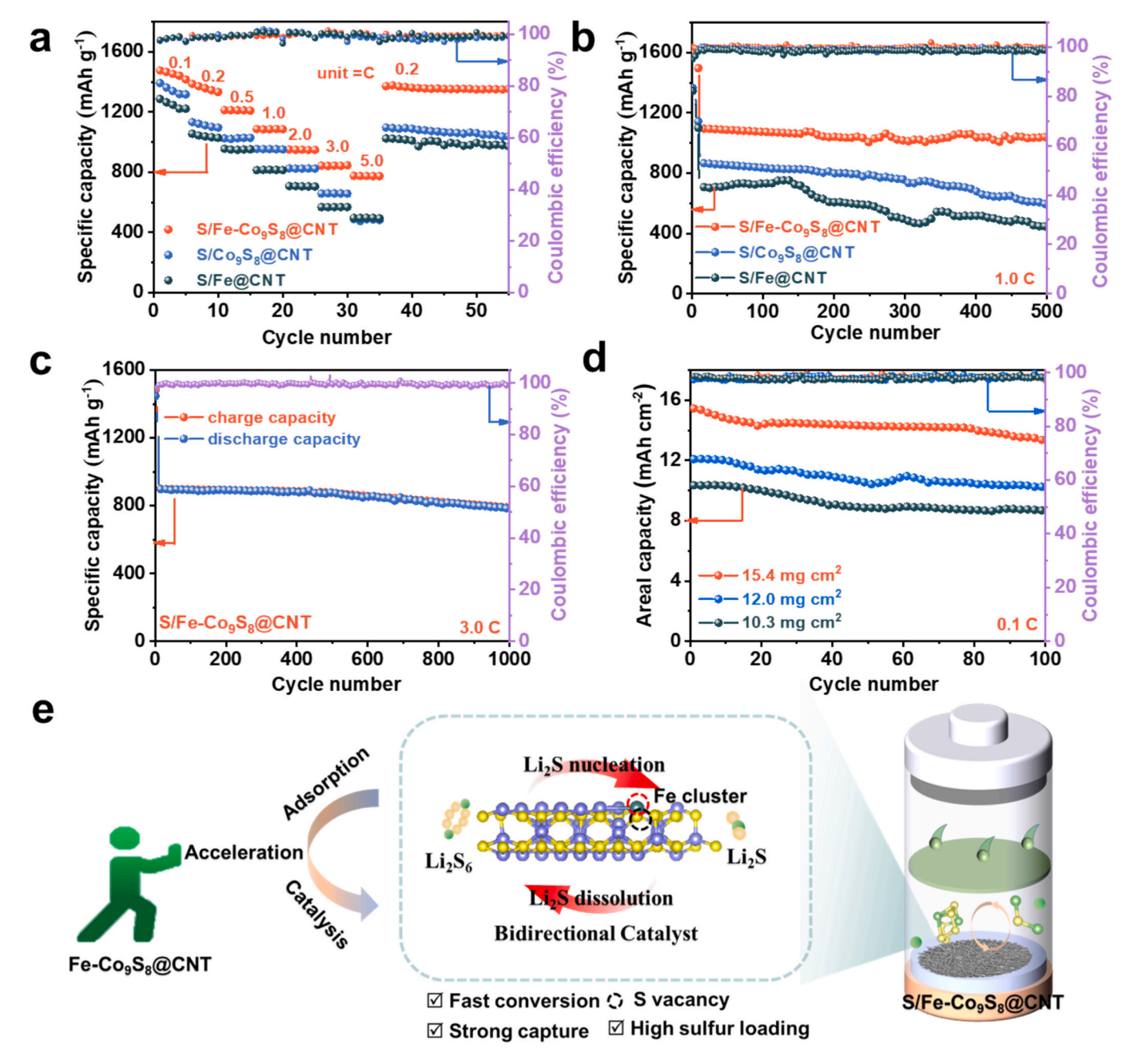


Fig. 7. (a) rate performance, and (b) cycling stability at 1.0C of three cathodes. (c) Long cycling performances at 3.0C of S/Fe-Co₉S₈@CNT cathode. (d) The areal capacity of S/Fe-Co₉S₈@CNT cathode with high-loading sulfur at 0.1C. (e) Schematic illustration of the Fe-Co₉S₈@CNT heterostructure restricts the shuttle of LiPSs and promotes bidirectional LiPSs conversion.

Hence, we test the performance of S/Fe-Co₉S₈@CNT cathode under S high loading of 5.9,7.5, and 8.2 mg cm⁻² and poor electrolyte/sulfur ratio (E/S is 7.0 μL mg⁻¹). In Fig. S28a, S/Fe-Co₉S₈@CNT cathode sitll expresses excellent area capacities of 7.3, 6.5, and 5.1 mAh cm⁻² over 100 cycles at 0.2C, respectively. When raising the S loading up to 10.3 and 12.0 mg cm⁻² with the E/S of 6.5 μL mg⁻¹(Fig. 7d), the S/Fe-Co₉S₈@CNT cathode still keeps remarkable preserved areal capacity of 10.2 and 8.7 mAh cm⁻² at 0.1 after 100 cycles, respectively. Even at much cruel circumstances (S loading of 15.4 mg cm⁻² with the E/S of 6.0 μL mg⁻¹), S/Fe-Co₉S₈@CNT cathode still has the outstanding initial areal capacity (15.44 mAh cm⁻²) and reservation capacity of 13.41 mAh cm⁻² over 100 cycles. Additionally, corresponding GCD profiles still show two clear voltage platforms (Fig. S28b), demonstrating that the superior electrochemical property of Fe-Co₉S₈@CNT is well maintained at high S loading.

Combine all of the above analysis, it can be concluded that Fe-Co₉S₈@CNT as S host for LSBs exhibits the remarkable performance, which even can surpass many Co₉S₈-based cathodes reported in the literature, especially in achieving high areal capacity with low electrolyte (Table S8). As depicted in Fig. 7e, the high LSBs performance are mainly from following reasons: (1) hollow CNT with well-developed pore distribution boost charge/mass transfer and provide rich room to load S; (2) the formation of Fe-Co bonds induces many V_S in Co₉S₈ to optimize the better e_g orbit exchange, which can display the more stable BO with all Li₂S_x thus can effectively capture LiPSs; (3) Fe-doping reduce the bandgap of Co₉S₈, thus lowering the ΔG of RDS and weaking the Li—S and S—S bonds to enhance the bidirectional conversion of LiPSs.

4. Conclusion

In conclusion, we successfully designed hollow CNT supported Fe modified Co₉S₈ as efficient S host for LSBs. The hollow CNT offers steady frameworks, which not only can help to increase S loading, but also can enhance electron/mass transfer. Further DFT calculation, NBO, and XAFS confirm that Fe doped into Co₉S₈ induces lower e_g orbit occupancy of Co sites to enable the stable BOs with all Li₂S_x, thus efficiently boosting the S conversion kinetics and significantly inhibiting "shuttle effect". Benefiting from these superiorities, the S/Fe-Co₉S₈@CNT cathode achieves outstanding electrochemical properties in terms of stable cycle life and high rate. Even under 3.0C, S/Fe-Co₉S₈@CNT cathode still indicates favorable initial discharge capacity of 899.1 mAh g⁻¹) and superior cycling stability with an ultralow capacity attention of 0.022 % each cycle over 1000 cycles. In the poor E/S $(6.0 \,\mu\text{L mg}^{-1})$ and the high sulfur loading (15.4 mg cm⁻²), the S/Fe-Co₉S₈@CNT cathode can also keep remarkable initial areal capacity (15.44 mAh cm⁻²) and desirable cycle stability (13.41 mAh cm⁻²). In situ Raman further reveals that that the Fe-Co₂S₈@CNT can effectively solve the shuttle effect and accelerate the LiPSs redox kinetics. The findings of this study offer insights for further development of advanced cobalt-based cathodes for highcapacity and long-life LSBs.

CRediT authorship contribution statement

Wei Zhou: Writing – review & editing, Writing – original draft, Visualization, Validation, Methodology, Formal analysis, Data curation. Zilong Li: Investigation, Data curation. Shunlian Ning: Investigation, Data curation. Jinchang Xu: Validation, Investigation, Data curation. Ming-Hsien Lee: Validation, Investigation, Data curation. Dengke Zhao: Validation, Investigation, Data curation. Jian Qing: Investigation, Data curation. Nan Wang: Writing – review & editing, Methodology, Conceptualization. Hui Meng: Writing – review & editing, Validation, Resources, Investigation, Conceptualization.

Declaration of competing interest

The authors declare that they have no known competing financial interests or personal relationships that could have appeared to influence the work reported in this paper.

Acknowledgements

This work was supported by the National Natural Science Foundation of China (22478151 and 22209056), the Guangdong Basic and Applied Basic Research Foundation (2023A1515010270 and 2023A1515010921) and the Science and Technology Planning Project of Guangzhou, China (Grant No. 201605030008, SL2024A04J00672, 2025A04J5167), the Key Research & Development and Promotion Projects in Henan Province (242102241033).

Appendix A. Supplementary data

Additional SEM, XRD, TEM, BET, XPS, TGA and etc. for the studied catalysts and comparison samples; Fitting curves and parameters for Fe and Co K-edge EXAFS; WT of EXAFS data for comparison samples; Schematic diagram illustrating the optimal adsorption configuration of Li_2S_{x} ; The DOS for different samples; The table for comparison of electrochemical performance of S/Fe-Co₉S₈@CNT cathode with other sulfur cathodes. Supplementary data to this article can be found online at doi: https://doi.org/10.1016/j.cej.2025.167290.

Data availability

Data will be made available on request.

References

- [1] D. Tian, X. Song, M. Wang, X. Wu, Y. Qiu, B. Guan, X. Xu, L. Fan, N. Zhang, K. Sun, MoN supported on graphene as a bifunctional interlayer for advanced Li-S batteries, Adv. Energy Mater. 9 (2019) 1901940.
- [2] X. Lv, T. Lei, B. Wang, W. Chen, Y. Jiao, Y. Hu, Y. Yan, J. Huang, J. Chu, C. Yan, C. Wu, J. Wang, X. Niu, J. Xiong, An efficient separator with low Li-ion diffusion energy barrier resolving feeble conductivity for practical lithium-sulfur batteries, Adv. Energy Mater. 9 (2019) 1901800.
- [3] S. Li, W. Zhang, J. Zheng, M. Lv, H. Song, L. Du, Inhibition of polysulfide shuttles in Li-S batteries: modified separators and solid-state electrolytes, Adv. Energy Mater. 11 (2020) 2000779.
- [4] L. Jiao, C. Zhang, C. Geng, S. Wu, H. Li, W. Lv, Y. Tao, Z. Chen, G. Zhou, J. Li, G. Ling, Y. Wan, Q.H. Yang, Capture and catalytic conversion of polysulfides by in situ built TiO₂-MXene heterostructures for lithium-sulfur batteries, Adv. Energy Mater. 9 (2019) 1900219.
- [5] Q. Wang, H. Zhao, B. Li, C. Yang, M. Li, Y. Li, P. Han, M. Wu, T. Li, R. Liu, MOF-derived Co₉S₈ nano-flower cluster array modified separator towards superior lithium-sulfur battery, Chin. Chem. Lett. 32 (2021) 1157–1160.
- [6] J. He, Y. Chen, A. Manthiram, Vertical Co₉S₈ hollow nanowall arrays grown on a Celgard separator as a multifunctional polysulfide barrier for high-Prformance Li–S btteries, Energy Environ. Sci. 11 (2018) 2560–2568.
- [7] X. Yu, H. Wu, J.H. Koo, A. Manthiram, Tailoring the pore size of a polypropylene separator with a polymer having intrinsic nanoporosity for suppressing the polysulfide shuttle in lithium-sulfur batteries, Adv. Energy Mater. 10 (2019) 1902872.
- [8] L. Wang, Z. Hu, X. Wan, W. Hua, H. Li, Q.H. Yang, W. Wang, Li_2S_4 anchoring governs the catalytic sulfur reduction on defective SmMn₂O₅ in lithium-sulfur battery, Adv. Energy Mater. 12 (2022) 2200340.
- [9] B. Li, Q. Su, L. Yu, J. Zhang, G. Du, D. Wang, D. Han, M. Zhang, S. Ding, B. Xu, Tuning the band structure of MoS₂ via Co₉S₈@MoS₂ core-shell structure to boost catalytic activity for lithium-sulfur batteries, ACS Nano 14 (2020) 17285–17294.
- [10] H. Zhang, M. Zou, W. Zhao, Y. Wang, Y. Chen, Y. Wu, L. Dai, A. Cao, Highly dispersed catalytic $\rm Co_3S_4$ among a hierarchical carbon nanostructure for high-rate and long-life lithium-sulfur batteries, ACS Nano 13 (2019) 3982–3991.
- [11] Z. Bai, Z. Wang, T. Wang, Z. Wu, R. Li, X. Gao, Y. Bai, K. Sun, Deciphering the eg occupancy descriptor on perovskite oxides for lithium-sulfur batteries, Energy Storage Mater. 71 (2024) 103657.
- [12] W. Zhou, M. Chen, D. Zhao, C. Zhu, N. Wang, W. Lei, Y. Guo, L. Li, Engineering spin state in spinel Co3O4 nanosheets by V-doping for bidirectional catalysis of polysulfides in lithium–sulfur batteries, Adv. Funct. Mater. 34 (2024) 2402114.
- [13] Z. Zhou, L. Zhao, J. Wang, Y. Zhang, Y. Li, S. Shoukat, X. Han, Y. Long, Y. Liu, Optimizing E_g orbital occupancy of transition metal sulfides by building internal electric fields to adjust the adsorption of oxygenated intermediates for Li-O₂ batteries, Small 19 (2023) 2302598.
- [14] Y. Liu, C. Xiao, M. Lyu, Y. Lin, W. Cai, P. Huang, W. Tong, Y. Zou, Y. Xie, Ultrathin Co₂S₄ nanosheets that synergistically engineer spin states and exposed Polyhedra that promote water oxidation under neutral conditions, Angew. Chem. Int. Ed. 54 (2015) 11231–11235.
- [15] Wang, J., Xing, Z., Kang, R., Zheng, Y., Zhang, Z., Ma, T., Wang, Y., Yin, B., Liao, Y., Li, L., Cheng, C., Li, S. Metal nitride controlled atomic doping of Mox+ in NiFe (oxy)hydroxide to trigger lattice oxygen-mediated mechanism for superior oxygen evolution. Adv. Funct. Mater., n/a 2418439.
- [16] L. Wu, S. Li, L. Li, H. Zhang, L. Tao, X. Geng, H. Yang, W. Zhou, C. Sun, D. Ju, B. An, Modest modulation on the electronic structure of Co₉S₈ by vanadium doping for high-performance rechargeable Zn-air batteries, Appl. Catal. B, Environ. Energy 324 (2023) 122250.
- [17] G. Ma, X. Xu, Z. Feng, C. Hu, Y. Zhu, X. Yang, J. Yang, Y. Qian, Carbon-coated mesoporous Co958 nanoparticles on reduced graphene oxide as a long-life and high-rate anode material for potassium-ion batteries, Nano Res. 13 (2020) 802–809.
- [18] J. Zhou, X. Liu, J. Zhou, H. Zhao, N. Lin, L. Zhu, Y. Zhu, G. Wang, Y. Qian, Fully integrated hierarchical double-shelled Co₉S₈@CNT nanostructures with unprecedented performance for Li-S batteries, Nanoscale Horiz. 4 (2019) 182–189.
- [19] Z. Tong, L. Huang, H. Liu, W. Lei, H. Zhang, S. Zhang, Q. Jia, Defective graphitic carbon nitride modified separators with efficient polysulfide traps and catalytic sites for fast and reliable sulfur electrochemistry, Adv. Funct. Mater. 31 (2021) 2010455.
- [20] H. Gao, S. Miao, M. Shi, X. Mao, X. Zhu, In situ-formed cobalt nanoparticles embedded nitrogen-doped hierarchical porous carbon as sulfur host for highperformance Li-S batteries, Electrochim. Acta 403 (2022) 139717.
- [21] Y. Zhong, L. Yin, P. He, W. Liu, Z. Wu, H. Wang, Surface chemistry in cobalt phosphide-stabilized lithium-sulfur batteries, J. Am. Chem. Soc. 140 (2018) 1455–1459.
- [22] L. Qie, A. Manthiram, Uniform Li₂S precipitation on N,O-codoped porous hollow carbon fibers for high-energy-density lithium-sulfur batteries with superior stability, Chem. Commun. (Camb.) 52 (2016) 10964–10967.
- [23] H. Chen, W.-D. Dong, F.-J. Xia, Y.-J. Zhang, M. Yan, J.-P. Song, W. Zou, Y. Liu, Z.-Y. Hu, J. Liu, Y. Li, H.-E. Wang, L.-H. Chen, B.-L. Su, Hollow nitrogen-doped carbon/sulfur@MnO₂ nanocomposite with structural and chemical dualencapsulation for lithium-sulfur battery, Chem. Eng. J. 381 (2020) 122746.
- [24] L. Wu, C. Cai, X. Yu, Z. Chen, Y. Hu, F. Yu, S. Zhai, T. Mei, L. Yu, X. Wang, Scalable 3D honeycombed Co₃O₄ modified separators as Polysulfides barriers for highperformance Li-S batteries, ACS Appl. Mater. Interfaces 14 (2022) 35894–35904.
- [25] W. Tang, K. Teng, W. Guo, F. Gu, B. Li, R. Qi, R. Liu, Y. Lin, M. Wu, Y. Chen, Defectengineered Co₃O₄@nitrogen-deficient graphitic carbon nitride as an efficient

- bifunctional electrocatalyst for high-performance metal-air batteries, Small 18 (2022) 2202194.
- [26] C. Zhou, M. Li, N. Hu, J. Yang, H. Li, J. Yan, P. Lei, Y. Zhuang, S. Guo, Single-atom-regulated heterostructure of binary nanosheets to enable dendrite-free and kinetics-enhanced Li–S batteries, Adv. Funct. Mater. 32 (2022) 2204635.
- [27] X. Zhang, T. Yang, Y. Zhang, X. Wang, J. Wang, Y. Li, A. Yu, X. Wang, Z. Chen, Single zinc atom aggregates: synergetic interaction to boost fast polysulfide conversion in lithium-sulfur batteries, Adv. Mater. 35 (2023) 2208470.
- [28] C. Zhang, R. Du, J.J. Biendicho, M. Yi, K. Xiao, D. Yang, T. Zhang, X. Wang, J. Arbiol, J. Llorca, Y. Zhou, J.R. Morante, A. Cabot, Tubular CoFeP@CN as a Mott–Schottky catalyst with multiple adsorption sites for robust lithium–sulfur batteries, Adv. Energy Mater. 11 (2021) 2100432.
- [29] T. Liu, J. Li, H. Cui, Y. Liu, K. Liu, H. Wei, M. Wang, Tuning Li nucleation and growth via oxygen vacancy-enriched 3D flexible self-supporting protection layer of P-Mn₃O_{4-x} for advanced lithium-sulfur batteries, J. Energy Chem. 76 (2023) 339–348.
- [30] Z. Li, I. Sami, J. Yang, J. Li, R.V. Kumar, M. Chhowalla, Lithiated metallic molybdenum disulfide nanosheets for high-performance lithium-sulfur batteries, Nat. Energy 8 (2023) 84–93.
- [31] Z. Ye, Y. Jiang, T. Yang, L. Li, F. Wu, R. Chen, Engineering catalytic CoSe-ZnSe heterojunctions anchored on graphene aerogels for bidirectional sulfur conversion reactions, Adv. Sci. 9 (2021) 2103456.
- [32] S.H. Yang, J.M. Choi, R. Saroha, S.W. Cho, Y.C. Kang, J.S. Cho, Hollow porous carbon nanospheres containing polar cobalt sulfide (CooS₈) nanocrystals as electrocatalytic interlayers for the reutilization of polysulfide in Lithium-sulfur batteries, J. Colloid Interface Sci. 645 (2023) 33–44.
- [33] Q. Gong, L. Hou, T. Li, Y. Jiao, P. Wu, Regulating the molecular interactions in polymer binder for high-performance lithium–sulfur batteries, ACS Nano 16 (2022) 8449–8460.
- [34] J.-L. Yang, D.-Q. Cai, Q. Lin, X.-Y. Wang, Z.-Q. Fang, L. Huang, Z.-J. Wang, X.-G. Hao, S.-X. Zhao, J. Li, G.-Z. Cao, W. Lv, Regulating the Li₂S deposition by grain

- boundaries in metal nitrides for stable lithium-sulfur batteries, Nano Energy 91 (2022)
- [35] D. Zhang, Y. Luo, J. Liu, Y. Dong, C. Xiang, C. Zhao, H. Shu, J. Hou, X. Wang, M. Chen, ZnFe₂O₄-Ni₅P₄ Mott-Schottky heterojunctions to promote kinetics for advanced Li-S batteries, ACS Appl. Mater. Interfaces 14 (2022) 23546–23557.
- [36] W. Yao, W. Zheng, J. Xu, C. Tian, K. Han, W. Sun, S. Xiao, ZnS-SnS@NC heterostructure as robust lithiophilicity and sulfiphilicity mediator toward highrate and long-life lithium-sulfur batteries, ACS Nano 15 (2021) 7114–7130.
- [37] J. Xu, S. An, X. Song, Y. Cao, N. Wang, X. Qiu, Y. Zhang, J. Chen, X. Duan, J. Huang, W. Li, Y. Wang, Towards high performance Li-S batteries via sulfonaterich COF-modified separator, Adv. Mater. 33 (2021) 2105178.
- [38] J. Jin, J. Yin, H. Liu, B. Huang, Y. Hu, H. Zhang, M. Sun, Y. Peng, P. Xi, C.H. Yan, Atomic sulfur filling oxygen vacancies optimizes H absorption and boosts the hydrogen evolution reaction in alkaline media, Angew. Chem. Int. Ed. 60 (2021) 14117–14123.
- [39] W. Jing, Q. Tan, Y. Duan, K. Zou, X. Dai, Y. Song, M. Shi, J. Sun, Y. Chen, Y. Liu, Defect-rich single atom catalyst enhanced polysulfide conversion kinetics to upgrade performance of Li-S batteries, Small 19 (2023) 2204880.
- [40] R.R. Chen, Y. Sun, S.J.H. Ong, S. Xi, Y. Du, C. Liu, O. Lev, Z.J. Xu, Antiferromagnetic inverse spinel oxide LiCoVO₄ with spin-polarized channels for water oxidation, Adv. Mater. 32 (2020) 1907976.
- [41] Y. Duan, S. Sun, Y. Sun, S. Xi, X. Chi, Q. Zhang, X. Ren, J. Wang, S.J.H. Ong, Y. Du, L. Gu, A. Grimaud, Z.J. Xu, Mastering surface reconstruction of metastable spinel oxides for better water oxidation, Adv. Mater. 31 (2019) 1807898.
- [42] Z. Han, S. Zhao, J. Xiao, X. Zhong, J. Sheng, W. Lv, Q. Zhang, G. Zhou, H.M. Cheng, Engineering d-p orbital hybridization in single-atom metal-embedded threedimensional electrodes for Li-S batteries, Adv. Mater. 33 (2021) 2105947.
- [43] X. Liu, L. Zhao, H. Xu, Q. Huang, Y. Wang, C. Hou, Y. Hou, J. Wang, F. Dang, J. Zhang, Tunable cationic vacancies of cobalt oxides for efficient electrocatalysis in Li-O₂ batteries, Adv. Energy Mater. 10 (2020) 2001415.